

Thermodynamic model of oxide overgrowth on bare metals: Relaxation of growth strain by plastic deformation

F. Reichel, L. P. H. Jeurgens,* and E. J. Mittemeijer

Max Planck Institute for Metals Research, Heisenbergstraße 3, D-70569 Stuttgart, Germany

(Received 17 May 2006; published 17 October 2006)

A thermodynamic model has been developed which predicts the growth of either an initial (semi)coherent, strained crystalline oxide phase, or an initial amorphous oxide phase (with a possible amorphous-to-crystalline transition) on the bare single-crystalline metal substrate as a function of the metal substrate orientation, the growth temperature, and the oxide-film thickness. The model accounts for relaxation of residual stresses in a crystalline oxide overgrowth by plastic deformation (i.e., through the introduction of misfit dislocations at the metal/oxide interface). As an example, the microstructural evolution of the initial oxide film grown on the {111}, {110}, and {100} crystallographic surfaces of a bare Cr substrate has been modeled as a function of the growth temperature and the oxide-film thickness (<5 nm). The initial oxide-film growth on the bare Cr{100} and Cr{111} substrates is predicted to proceed by the initial formation and growth of an amorphous oxide film up to a critical thickness of about 0.5 and 0.9 nm, respectively. On the other hand, the onset of oxidation on a bare Cr{110} substrate should proceed by the direct overgrowth of a semicoherent, strained crystalline oxide film. These model predictions provide understanding for experimental observations reported in the literature.

DOI: [10.1103/PhysRevB.74.144103](https://doi.org/10.1103/PhysRevB.74.144103)

PACS number(s): 61.72.Lk, 68.55.Jk, 05.70.Np, 81.10.Aj

I. INTRODUCTION

Upon oxidation of a bare (i.e., without a native oxide), single-crystalline metal or semiconductor substrate, the microstructure of the developing oxide film can be variable. For metals (or semiconductors) such as Al, Si, Ta, an initially amorphous oxide film develops on the bare metal surface, which transforms into a crystalline oxide film if the thickness exceeds a critical value at higher temperatures (e.g., Refs. 1 and 2 and references therein). For other metals such as Cu, Ni, and Fe, oxidation starts with the nucleation and growth of a (semi-)coherent, elastically strained crystalline oxide film (e.g., Refs. 1 and 2 and references therein). After attaining some critical oxide-film thickness, the build-up growth strain in the oxide film is released by the formation of misfit dislocations (i.e., plastic deformation occurs), which are initiated at the metal/oxide interface.

For many technological applications (e.g., microelectronics, surface coatings, and catalysis), the growth of either an amorphous or a coherent, single-crystalline oxide film is desired, because of the absence of grain boundaries in both these types of oxide films.³⁻⁵ Grain boundaries in the grown oxide films may act as paths for fast atom or electron transport, thereby deteriorating material properties such as the electrical resistivity, corrosion resistance, or catalytic activity.^{2,6} In particular for technological applications in the field of microelectronics, thin amorphous oxide films are required, because of their uniform thickness and specific microstructure (no grain boundaries, moderate bond flexibility, large free volume, negligible growth strain) and related properties (e.g., passivating oxide-film growth kinetics, low leakage current, high dielectric constant, high corrosion resistance).^{2,3,5}

As shown by recent model calculations by Jeurgens *et al.*¹ on the relative thermodynamic stability of an amorphous oxide film on its metal substrate (with respect to that of the corresponding elastically strained, crystalline oxide film on

the same substrate), an amorphous structure for the initially grown oxide film can be thermodynamically (instead of kinetically) preferred due to the lower sum of the interfacial and surface energies for the amorphous-oxide-film/metal-substrate configuration as compared to the crystalline-oxide-film/metal-substrate configuration. However, in this model, which was applied to the oxidation of Al, the possible relaxation of growth strain in the crystalline oxide overgrowth (and/or the parent metal substrate) by introduction of misfit dislocations at the metal/oxide interface is not considered, which is only justified up to a certain oxide-film thickness and for a small initial lattice mismatch between the metal substrate and the oxide overgrowth.

In the present contribution, the original model description¹ has been extended and thereby improved considerably to account for the relaxation of growth strain (originating from the initial lattice mismatch between a crystalline oxide overgrowth and its parent metal substrate) by plastic deformation. The resulting model can be applied to distinctly larger oxide-film thicknesses, as well as to metal/oxide systems of high initial lattice mismatch. A general expression has been derived for the assessment of the energy of the interface between a metal substrate and its corresponding coherent or semicoherent crystalline oxide overgrowth. Further, the different approaches as reported in the literature for the estimation of the misfit-dislocation energy contribution to the interface energy have been outlined and a numerical procedure has been presented to calculate the value of the interface energy of the corresponding semicoherent interface as function of the growth temperature and oxide-film thickness.

The new model description has been applied to the Cr/Cr₂O₃ system, which not only represents a case of very large lattice mismatch, but also exhibits pronouncedly different mismatches along different directions in the boundary plane between the metal substrate and the oxide film (i.e., the crystalline oxide film exhibits anisotropic growth strain). On the basis of the model calculations, the thermodynamic sta-

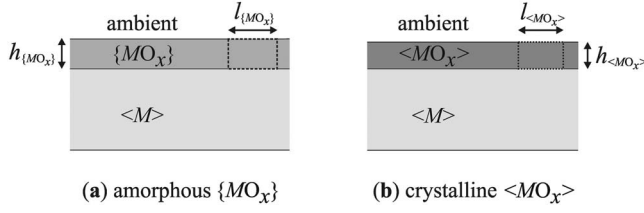


FIG. 1. Schematic drawing of a homogeneous MO_x oxide film of uniform thickness, h_{MO_x} , on top of its single crystalline metal substrate, $\langle M \rangle$, in contact with the ambient (e.g., vacuum, a gas atmosphere or an adsorbed layer). (a) the case of an amorphous oxide film $\{MO_x\}$ of uniform thickness, $h_{\{MO_x\}}$, on the $\langle M \rangle$ substrate, while (b) the case of the corresponding crystalline oxide film $\langle MO_x \rangle$ of uniform thickness, $h_{\langle MO_x \rangle}$, on the $\langle M \rangle$ substrate. Both films have been formed from the same molar quantity of oxygen on identical substrates. The two competing cells of volume $h_{\{MO_x\}} \times l_{\{MO_x\}}^2$ and $h_{\langle MO_x \rangle} \times l_{\langle MO_x \rangle}^2$, as indicated in (a) and (b), respectively, contain the same molar quantity of oxide.

bility of an amorphous Cr_2O_3 film on different crystallographic faces of the Cr substrate, as compared to that of the corresponding crystalline Cr_2O_3 film on the same crystallographic faces of the Cr substrate, has been evaluated as function of the growth conditions. Finally, the model predictions for the microstructural evolution of thin oxide films grown on bare, single-crystalline Cr substrates have been compared with experimental observations as obtained by low energy electron diffraction (LEED),⁷⁻⁹ reflection high energy electron diffraction (RHEED),^{7,10,11} x-ray scattering¹² and valence band spectra of the oxidized metal as recorded by ultraviolet (UPS), and x-ray photoelectron spectroscopy (XPS).¹³

II. THEORY

A. Basis of the model

Consider an homogeneous oxide film, MO_x , of uniform thickness, h_{MO_x} , on its single-crystalline metal substrate, $\langle M \rangle$. In one case, the oxide film is amorphous, denoted as $\{MO_x\}$, with thickness $h_{\{MO_x\}}$. In the other case, the oxide film is crystalline, denoted as $\langle MO_x \rangle$, with thickness $h_{\langle MO_x \rangle}$. The braces $\{$ and the brackets \langle refer to the amorphous state and the crystalline state, respectively. The composition of the amorphous and crystalline oxides is the same, and both films have been formed from the same molar quantity of oxygen on identical substrates.

To assess the thermodynamic stability of the amorphous oxide film on the metal substrate with respect to that of the corresponding crystalline oxide film on the metal substrate, the energetics of the $\langle M \rangle$ - $\{MO_x\}$ and $\langle M \rangle$ - $\langle MO_x \rangle$ configurations will be compared for cells of volume $h_{\{MO_x\}} \times l_{\{MO_x\}}^2$ and $h_{\langle MO_x \rangle} \times l_{\langle MO_x \rangle}^2$, respectively [see Figs. 1(a) and 1(b)]. Both cells contain the same molar quantity of oxide. The difference in total Gibbs energy between the amorphous and crystalline cells, $\Delta G = G_{\{MO_x\}} - G_{\langle MO_x \rangle}$, can be given as

$$\Delta G = h_{\{MO_x\}} \left(\frac{\Delta G_{\{MO_x\}}^f - \Delta G_{\langle MO_x \rangle}^f}{V_{\{MO_x\}}} \right) + \gamma_{\{MO_x\}\text{-amb}} + \gamma_{\langle M \rangle\text{-}\{MO_x\}} - \chi (\gamma_{\langle MO_x \rangle\text{-amb}} + \gamma_{\langle M \rangle\text{-}\langle MO_x \rangle}), \quad (1)$$

where $\Delta G_{\{MO_x\}}^f$ and $\Delta G_{\langle MO_x \rangle}^f$ are the Gibbs free energies of formation of the amorphous and the crystalline oxide, respectively; $V_{\{MO_x\}}$ is the molar volume of the amorphous oxide; $\gamma_{\{MO_x\}\text{-amb}}$ and $\gamma_{\langle MO_x \rangle\text{-amb}}$ are the surface energies of the amorphous oxide and the crystalline oxide in contact with the ambient, respectively; $\gamma_{\langle M \rangle\text{-}\{MO_x\}}$ and $\gamma_{\langle M \rangle\text{-}\langle MO_x \rangle}$ are the interfacial energies of the interface between the metal substrate and the amorphous oxide and the metal substrate and the crystalline oxide, respectively; χ denotes the ratio of the surface areas of the unstrained amorphous cell and the (strained) crystalline cell (see Sec. II B and Ref. 1)

$$\chi = \frac{l_{\{MO_x\}}^2}{l_{\langle MO_x \rangle}^2}. \quad (2)$$

If $\Delta G < 0$ the amorphous oxide cell is more stable, whereas for $\Delta G > 0$ the crystalline oxide cell is more stable.

B. Interfacial energies

Experimental values for the solid-solid interfacial energies between a metal substrate and its amorphous or crystalline oxide overgrowth [i.e., values for $\gamma_{\langle M \rangle\text{-}\{MO_x\}}$ and $\gamma_{\langle M \rangle\text{-}\langle MO_x \rangle}$ in Eq. (1)] as function of the growth conditions are generally not available. Therefore approximative expressions have been derived on the basis of the macroscopic atom approach.¹⁴

The *crystalline-amorphous* interface $\langle M \rangle$ - $\{MO_x\}$ is conceived as an interface between a crystalline solid (i.e., metal $\langle M \rangle$) and a configurationally frozen liquid (as a model for the amorphous oxide, $\{MO_x\}$). Because of the relatively large free volume and moderate bond flexibility of an amorphous phase, it is assumed that no mismatch strain resides in the amorphous oxide film (and consequently the metal substrate) at the oxide-growth temperature. It then follows that the energy, $\gamma_{\langle M \rangle\text{-}\{MO_x\}}$, of the interface between the metal substrate and the amorphous oxide film (per unit area of the interface) can be expressed as the resultant of three additive energy contributions (for details, see Ref. 1), i.e.

$$\gamma_{\langle M \rangle\text{-}\{MO_x\}} = \gamma_{\langle M \rangle\text{-}\{MO_x\}}^{\text{interaction}} + \gamma_{\langle M \rangle\text{-}\{MO_x\}}^{\text{entropy}} + \gamma_{\langle M \rangle\text{-}\{MO_x\}}^{\text{enthalpy}}. \quad (3)$$

The (relatively large) negative interaction contribution, $\gamma_{\langle M \rangle\text{-}\{MO_x\}}^{\text{interaction}}$, arises from the chemical bonding between the amorphous oxide and the metal substrate across the interface. The positive entropy contribution, $\gamma_{\langle M \rangle\text{-}\{MO_x\}}^{\text{entropy}}$, results from the ordering (i.e., the decrease of configurational entropy) of the amorphous oxide near the interface with the crystalline metal substrate (for experimental confirmation see Ref. 15). Finally, the (relatively small) positive enthalpy contribution arises from the relative increase in enthalpy of the metal substrate atoms at the interface (as compared to the bulk) due to the liquid type of bonding with the amorphous oxide at the interface (see further Ref. 1).

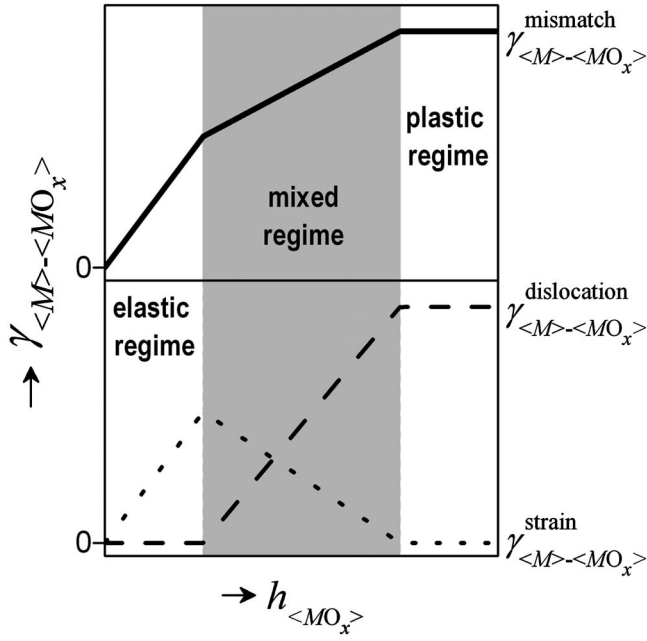


FIG. 2. Schematic drawing of the separate energy contributions due to (i) residual homogeneous strain, $\gamma_{\langle M \rangle - \langle MO_x \rangle}^{\text{strain}}$, and (ii) misfit dislocations, $\gamma_{\langle M \rangle - \langle MO_x \rangle}^{\text{dislocation}}$, to the total mismatch energy, $\gamma_{\langle M \rangle - \langle MO_x \rangle}^{\text{mismatch}}$, as function of crystalline oxide-film thickness $h_{\langle MO_x \rangle}$ in the various growth regimes. The elastic, mixed, and plastic regimes, as defined in Sec. II B have been indicated.

The energy, $\gamma_{\langle M \rangle - \langle MO_x \rangle}$, of the coherent or semicoherent *crystalline-crystalline* interface, $\langle M \rangle - \langle MO_x \rangle$, is the resultant of two energy contributions

$$\gamma_{\langle M \rangle - \langle MO_x \rangle} = \gamma_{\langle M \rangle - \langle MO_x \rangle}^{\text{interaction}} + \gamma_{\langle M \rangle - \langle MO_x \rangle}^{\text{mismatch}}. \quad (4a)$$

The interaction contribution, $\gamma_{\langle M \rangle - \langle MO_x \rangle}^{\text{interaction}}$, represents the chemical interaction between the crystalline oxide film and the metal substrate across the interface (see also above) and the mismatch contribution, $\gamma_{\langle M \rangle - \langle MO_x \rangle}^{\text{mismatch}}$, is due to the mismatch between the lattices of the metal substrate and the crystalline oxide film at the interface plane.

For a fully coherent crystalline-crystalline interface, $\langle M \rangle - \langle MO_x \rangle$, all lattice mismatch is accommodated fully elastically by the thin, epitaxially grown oxide film. This limiting case, which results in a homogeneous strain¹⁶ in the epitaxial oxide film, will be further referred to as the “*elastic regime*” (Fig. 2). With increasing oxide film thickness, as well as initially for $\langle M \rangle - \langle MO_x \rangle$ systems of large initial lattice mismatch (larger than, say, $\sim 7\%$), any homogeneous mismatch/growth strain in the crystalline oxide film may partly or fully be relaxed by built-in misfit dislocations at the metal/oxide interface (see Refs. 17 and 18). This intermediate case is characterized by a residual homogeneous strain and misfit dislocations in the crystalline oxide film and will be further referred to as the “*mixed regime*” (Fig. 2). Upon further increase of the oxide-film thickness, more and more misfit dislocations are generated at the semicoherent $\langle M \rangle - \langle MO_x \rangle$ interface in the crystalline oxide film until all residual strain within the grown oxide film has been fully relaxed. Then the

(fully) “*plastic regime*” has been entered (see Fig. 2).

The relaxation of growth strain in the crystalline oxide film by the generation of dislocations (plastic deformation) is accounted for by substituting the original mismatch contribution, $\gamma_{\langle M \rangle - \langle MO_x \rangle}^{\text{mismatch}}$, in Eq. (4a) (as introduced in Ref. 1) by two separate energy contributions $\gamma_{\langle M \rangle - \langle MO_x \rangle}^{\text{strain}}$ and $\gamma_{\langle M \rangle - \langle MO_x \rangle}^{\text{dislocation}}$ due to the residual homogeneous strain and the induced misfit dislocations in the crystalline oxide film, respectively. Hence [see Eq. (4a)]

$$\gamma_{\langle M \rangle - \langle MO_x \rangle} = \gamma_{\langle M \rangle - \langle MO_x \rangle}^{\text{interaction}} + \gamma_{\langle M \rangle - \langle MO_x \rangle}^{\text{strain}} + \gamma_{\langle M \rangle - \langle MO_x \rangle}^{\text{dislocation}}. \quad (4b)$$

In the mixed regime the residual homogeneous strain can thought to be superimposed on the periodic, inhomogeneous strain field, resulting from the sum of strain fields associated with each of the misfit dislocations. With increasing density of misfit dislocations at the semicoherent $\langle M \rangle - \langle MO_x \rangle$ interface, the strain contribution, $\gamma_{\langle M \rangle - \langle MO_x \rangle}^{\text{strain}}$, decreases, whereas the dislocation term, $\gamma_{\langle M \rangle - \langle MO_x \rangle}^{\text{dislocation}}$, increases (see Fig. 2 and e.g., Ref. 18). Because the energy contributions due to the residual homogeneous strain and the misfit dislocations in the crystalline oxide film are attributed (here) to the interface energy instead of to the bulk energy of the film [see Eq. (1) in Sec. II A], the interface energy $\gamma_{\langle M \rangle - \langle MO_x \rangle}$ exhibits a pronounced dependence on the oxide-film thickness (see Fig. 2).

The interaction energy contribution, $\gamma_{\langle M \rangle - \langle MO_x \rangle}^{\text{interaction}}$, per unit area of the $\langle M \rangle - \langle MO_x \rangle$ interface [see Eq. (4b)] is given by

$$\gamma_{\langle M \rangle - \langle MO_x \rangle}^{\text{interaction}} = \frac{p \Delta H_{\text{O in} \langle M \rangle}^{\infty}}{A_{\langle O \rangle}^{\text{unstr}}} (1 + \bar{\epsilon}_{11})(1 + \bar{\epsilon}_{22}), \quad (4c)$$

where p is a constant fraction that depends on the shape of the Wigner-Seitz cell of oxygen in the oxide (*here*: $p = \frac{1}{3}$; see Ref. 1); $\Delta H_{\text{O in} \langle M \rangle}^{\infty}$ denotes the enthalpy of mixing at infinite dilution of 1-mol O(g) atoms in the solid crystalline metal $\langle M \rangle$; the molar interface area $A_{\langle O \rangle}^{\text{unstr}}$ is defined as the area of the $\langle M \rangle - \langle MO_x \rangle$ interface containing 1-mol O atoms for the case of the *unstrained* crystalline oxide film, which differs from the corresponding molar interface area $A_{\langle O \rangle}$ in the original treatment,¹ as defined for the *strained* crystalline oxide film. To correct for the area difference between the strained and unstrained crystalline oxide film, the term $(1 + \bar{\epsilon}_{11})(1 + \bar{\epsilon}_{22})$ is introduced here, where $\bar{\epsilon}_{11}$ and $\bar{\epsilon}_{22}$ denote the *residual*, homogeneous, normal strains in the oxide in perpendicular directions 1 and 2, respectively, at the $\langle M \rangle - \langle MO_x \rangle$ interface plane.

The strain energy $\gamma_{\langle M \rangle - \langle MO_x \rangle}^{\text{strain}}$ due to the *residual* homogeneous strain in the crystalline oxide film, is obtained from

$$\gamma_{\langle M \rangle - \langle MO_x \rangle}^{\text{strain}} = h_{\langle MO_x \rangle} \bar{\sigma}_{ij} \bar{\epsilon}_{ij} = h_{\langle MO_x \rangle} C_{ijkl} \bar{\epsilon}_{ij} \bar{\epsilon}_{kl} \quad (i, j, k, l = 1, 2, 3), \quad (4d)$$

where $\bar{\sigma}_{ij}$ is the stress tensor, C_{ijkl} is the fourth-rank stiffness tensor, and $\bar{\epsilon}_{ij}$ is the *residual* homogeneous strain tensor of $\langle MO_x \rangle$. The perpendicular directions 1 and 2 are parallel to the $\langle M \rangle - \langle MO_x \rangle$ interface plane, whereas direction 3 is perpendicular to the interface plane.

The *initial* lattice mismatch within the $\langle M \rangle$ - $\langle MO_x \rangle$ interface plane is characterized by the mismatch values f_1 and f_2 in the two perpendicular directions 1 and 2 within the interface plane

$$f_i = \frac{{}^i a_{\langle M \rangle} - {}^i a_{\langle MO_x \rangle}}{{}^i a_{\langle MO_x \rangle}} \quad (i=1,2), \quad (5a)$$

where ${}^i a_{\langle M \rangle}$ and ${}^i a_{\langle MO_x \rangle}$ denote values of *unstrained* lattice spacings corresponding to direction 1 and 2 of the metal substrate $\langle M \rangle$ and the $\langle MO_x \rangle$ film, respectively. For the case of a semicoherent $\langle M \rangle$ - $\langle MO_x \rangle$ interface in the mixed regime (see Fig. 2), the *residual* normal strains, $\bar{\epsilon}_{ii}$, within the $\langle MO_x \rangle$ film in directions 1 and 2 depend on the corresponding *residual* lattice spacings, ${}^i \bar{a}_{\langle MO_x \rangle}$, of the $\langle MO_x \rangle$ film according to

$$\bar{\epsilon}_{ii} = \frac{{}^i \bar{a}_{\langle MO_x \rangle} - {}^i a_{\langle MO_x \rangle}}{{}^i a_{\langle MO_x \rangle}} \quad (i=1,2). \quad (5b)$$

Finally, the contribution of the dislocation energy, $\gamma_{\langle M \rangle\text{-}\langle MO_x \rangle}^{\text{dislocation}}$, to the total interface energy, $\gamma_{\langle M \rangle\text{-}\langle MO_x \rangle}$ in Eq. (4b), equals the sum of the total energies of the arrays of misfit dislocations, ${}^1 \gamma_{\langle M \rangle\text{-}\langle MO_x \rangle}^{\text{dislocation}}$ and ${}^2 \gamma_{\langle M \rangle\text{-}\langle MO_x \rangle}^{\text{dislocation}}$, with Burgers vectors parallel to directions 1 and 2, respectively

$$\gamma_{\langle M \rangle\text{-}\langle MO_x \rangle}^{\text{dislocation}} = {}^1 \gamma_{\langle M \rangle\text{-}\langle MO_x \rangle}^{\text{dislocation}} + {}^2 \gamma_{\langle M \rangle\text{-}\langle MO_x \rangle}^{\text{dislocation}}. \quad (4e)$$

In Sec. II C various treatments are outlined to estimate the misfit-dislocation energy terms ${}^i \gamma_{\langle M \rangle\text{-}\langle MO_x \rangle}^{\text{dislocation}}$ ($i=1,2$).

C. Misfit-dislocation energy

1. The semi-infinite overgrowth (SIO) approach

In the Frank-van der Merwe approach (e.g., Refs. 18 and 19) the energy of an array of misfit dislocations at a semicoherent solid-solid interface is calculated by adopting an interfacial force between the atoms on each side of the interface that varies periodically with the atomic disregistry (e.g., Refs. 18 and 19).

In the semi-infinite overgrowth (SIO) approach, the limiting case of a semi-infinite (i.e., infinitely thick) overgrowth (*here*: the $\langle MO_x \rangle$ oxide film) on top of a semi-infinite substrate (*here*: the metal substrate $\langle M \rangle$) is considered. Accordingly, all mismatch is assumed to be fully compensated by a rectangular grid of misfit dislocations at the interface, i.e., only the plastic regime is considered. Further, a sinusoidal interfacial potential energy density function between the substrate with lattice spacings ${}^1 a_{\langle M \rangle}$ and ${}^2 a_{\langle M \rangle}$ and the overgrowth with lattice spacings ${}^1 a_{\langle MO_x \rangle}$ and ${}^2 a_{\langle MO_x \rangle}$ is adopted that is a function of the relative displacements of the atoms on either side of the interface with respect to their equilibrium positions in the unstrained case. Additional assumptions of the SIO approach are listed in Table I.

The periodic distance, d_i , between adjacent, parallel misfit dislocations at the interface is equal to the vernier period of the mismatch, P_i , as defined in units of the lattice spacing of the overgrowth

$$d_i = P_i {}^i a_{\langle MO_x \rangle} = (P_i \pm 1) {}^i a_{\langle M \rangle} \quad (i=1,2). \quad (6a)$$

Then, a reference lattice with lattice spacings c_i ($i=1,2$) can be defined by

$$d_i = \left(P_i \pm \frac{1}{2} \right) c_i \quad (i=1,2) \quad (6b)$$

with

$$c_i = \frac{2 {}^i a_{\langle M \rangle} {}^i a_{\langle MO_x \rangle}}{{}^i a_{\langle M \rangle} + {}^i a_{\langle MO_x \rangle}} \quad (i=1,2). \quad (6c)$$

Accordingly, the lattices of the metal substrate, $\langle M \rangle$, and the crystalline oxide film, $\langle MO_x \rangle$, can be conceived as generated from the reference lattice by a homogeneous compression or a homogeneous expansion equal to $\frac{1}{2} c_i$ of the span $(P_i + 1)c_i$ or $P_i c_i$, respectively.¹⁸

The maximum amplitude W_0 of the interfacial potential energy density function determines the maximum interfacial force for disregistered atoms on each side of the interface and depends on the strength of bonding between the adjacent solids and hence on the adhesion energy. Estimations for W_0 based on simple bond concepts lead to the value of one third of the adhesion energy, $\gamma_{\langle M \rangle\text{-}\langle MO_x \rangle}^{\text{adhesion}}$,^{18,20} i.e.

$$W_0 = \frac{1}{3} \gamma_{\langle M \rangle\text{-}\langle MO_x \rangle}^{\text{adhesion}} = \frac{1}{3} (\gamma_{\langle M \rangle\text{-}amb} + \gamma_{\langle MO_x \rangle\text{-}amb} - \gamma_{\langle M \rangle\text{-}\langle MO_x \rangle}^{\text{interaction}}), \quad (6d)$$

where $\gamma_{\langle M \rangle\text{-}amb}$ and $\gamma_{\langle MO_x \rangle\text{-}amb}$ are the surface energies of the metal $\langle M \rangle$ and the crystalline oxide $\langle MO_x \rangle$ in contact with the ambient (see Sec. II A) and the interaction energy $\gamma_{\langle M \rangle\text{-}\langle MO_x \rangle}^{\text{interaction}}$ as defined in Sec. II B. Further, the interfacial shear modulus μ_i is related to the amplitude W_0 by¹⁸

$$\mu_i = \frac{2\pi W_0}{c_i} \quad (i=1,2). \quad (6e)$$

This results in the following expression for the energy ${}^i \gamma_{\langle M \rangle\text{-}\langle MO_x \rangle}^{\text{dislocation}}$ of an array of misfit dislocations with a Burgers vector parallel to direction i , per unit area of the semicoherent $\langle M \rangle$ - $\langle MO_x \rangle$ interface, according to the SIO approach¹⁸

$${}^i \gamma_{\langle M \rangle\text{-}\langle MO_x \rangle}^{\text{dislocation}} = \frac{\mu_i c_i}{4\pi^2} \left\{ \frac{1}{2} \left[1 + \left(\frac{1}{2} \beta_i - 1 \right) B_i - \beta_i \ln(1 - B_i^2) \right] \right\} \quad (i=1,2). \quad (7a)$$

The parameter B_i in Eq. (7a) is defined as

$$B_i = \sqrt{1 + \beta_i^2} - \beta_i \quad (i=1,2), \quad (7b)$$

with

$$\beta_i = \frac{2\pi\lambda c_i}{d_i \mu_i} \quad (i=1,2). \quad (7c)$$

The parameter λ in Eq. (7c) expresses the average elastic properties of the substrate-overgrowth system according to

TABLE I. Assumptions made in the semi-infinite overgrowth (SIO), large dislocation distance (LDD), extrapolation (EXTR), first approximation (APPR), Ball (BALL), and Volterra (VOLT) approaches, for estimation of the misfit-dislocation energy (see Sec. II C). The approximate thickness range (in oxide monolayers; ML) for which an approach is valid has also been indicated.

Assumption	SIO	LDD	EXTR	APPR	BALL	VOLT
$\langle M \rangle$ and $\langle MO_x \rangle$ phase:						
Initial dislocations present	no	no	no	no	no	no
Hookeian behavior (outside dislocation core)	yes	yes	yes	yes	yes	yes
Isotropic	yes	yes	yes	yes	yes	yes
Dislocations:						
Long and straight	yes	yes	yes	yes	yes	yes
Located at the interface	yes	yes	yes	yes	yes	yes
Only edge character	yes	yes	yes	yes	yes	no
Burgers vectors in interface plane	yes	yes	yes	yes	yes	no
Arranged in a rectangular grid	yes	yes	yes	yes	yes	yes
Regularly spaced	yes	yes	yes	yes	yes	yes
Dislocation core energy included	no	no	no	no	no	yes
Interactions at crossings of dislocation lines	no	no	no	no	no	no
Same dislocation energy as in bulk	no	no	no	no	no	yes
$\langle M \rangle$ - $\langle MO_x \rangle$ interface:						
Atomically smooth interface	yes	yes	yes	yes	yes	yes
Normal stress in interface plane	no	no	no	no	no	no
Strain gradient perpendicular to interface plane	yes	yes	yes	yes	no	yes
Interaction of dislocations with surface	no	no	yes	yes	yes	yes
Approximate thickness range (ML)	∞	>20	>10	several	<10	>20

$$\frac{1}{\lambda} = \frac{1 - \nu_{\langle M \rangle}}{\mu_{\langle M \rangle}} + \frac{1 - \nu_{\langle MO_x \rangle}}{\mu_{\langle MO_x \rangle}}, \quad (7d)$$

where $\mu_{\langle M \rangle}$ and $\mu_{\langle MO_x \rangle}$ and $\nu_{\langle M \rangle}$ and $\nu_{\langle MO_x \rangle}$ are the shear moduli and the Poisson constants of the metal substrate, $\langle M \rangle$, and the oxide overgrowth, $\langle MO_x \rangle$, respectively.

The energy term $\gamma_{\langle M \rangle - \langle MO_x \rangle}^{\text{dislocation}}$ according to Eq. (7a) incorporates the energy of disregistry at the interface, as well as the energy of the localized, inhomogeneous strain fields around each misfit dislocation (as is also the case for the following approaches presented in Secs. II C 2, II C 3, II C 4, II C 5, and II C 6). In the SIO approach, the strain field radius of the dislocations is taken equal to half of the dislocation spacing (i.e., $\frac{1}{2}d_i$).

2. The large dislocation distance (LDD) approach

For very small initial lattice mismatches and thick overgrowths (more than 20 atom layers), the expression for the dislocation energy as obtained using the SIO approach for the case of a semi-infinite overgrowth on a semi-infinite substrate [see Eq. (7a) in Sec. II C 1] can also be used to estimate the corresponding dislocation energy if the overgrowth is of *finite* thickness. Further assumptions of this so-called

large dislocation distance (LDD) approach are listed in Table I.

Since residual homogeneous strain can be present in an overgrowth of finite thickness, the unstrained lattice spacing $a_{\langle MO_x \rangle}^i$ of the overgrowth in Eqs. (6a)–(6c) of the SIO approach in Sec. II C 1 has to be replaced by the residual strain affected lattice spacing $\bar{a}_{\langle MO_x \rangle}^i$, which also influences the calculated constants μ_i , B_i , and β_i [see Eqs. (6e), (7b), and (7c), respectively]. Further, for thick overgrowths with large dislocation distances d_i , it is assumed that $\frac{c_i^2}{d_i^2} \approx 0$. This results in the following expression for the energy $\gamma_{\langle M \rangle - \langle MO_x \rangle}^{\text{dislocation}}$ of an array of misfit dislocations with a Burgers vector parallel to direction i , per unit area of the semicoherent $\langle M \rangle$ - $\langle MO_x \rangle$ interface, according to the LDD approach²¹

$$\gamma_{\langle M \rangle - \langle MO_x \rangle}^{\text{dislocation}} = \frac{\lambda c_i^2}{2\pi d_i} \left[\ln \left(\frac{\mu_i d_i}{4\pi \lambda c_i} \right) + 1 \right] \quad (i = 1, 2). \quad (8)$$

3. The extrapolation (EXTR) approach

The SIO model for the case of a semi-infinite overgrowth [see Eq. (7a) in Sec. II C 1] can be extrapolated to the case of a thin overgrowth of finite thickness, $h_{\langle MO_x \rangle}$, by adopting the so-called extrapolation (EXTR) approach. Then, as for the

LDD approach in Sec. II C 2, the unstrained lattice spacing $a_{\langle MO_x \rangle}$ of the overgrowth has to be replaced by the residual strain affected lattice spacing $\bar{a}_{\langle MO_x \rangle}$. However, in the EXTR approach the interactions of the individual strain fields of the dislocations with each other and with the free surface are now approximately accounted for (see Table I) by defining an effective range for the strain field of a dislocation. In the SIO approach, the strain field radius of the dislocations is taken equal to half of the dislocation spacing (i.e., $\frac{1}{2}d_i$), whereas in the EXTR approach the strain field radius is taken equal to $\frac{1}{2}q_i$,²² which is defined by

$$q_i = \begin{cases} \frac{4h_{\langle MO_x \rangle}d_i^2}{d_i^2 + 4h_{\langle MO_x \rangle}^2}; & d_i \geq 2h_{\langle MO_x \rangle} \\ d_i; & d_i \leq 2h_{\langle MO_x \rangle} \end{cases} \quad (i=1,2). \quad (9a)$$

This results in the following expression for the energy $\gamma_{\langle M \rangle - \langle MO_x \rangle}^{\text{dislocation}}$ of an array of misfit dislocations with a Burgers vector parallel to direction i , per unit area of the semicoherent $\langle M \rangle - \langle MO_x \rangle$ interface, according to the EXTR approach²²

$$\gamma_{\langle M \rangle - \langle MO_x \rangle}^{\text{dislocation}} = \frac{\mu_i c_i}{8\pi^2} (1 - B_i + \beta_i B_i) + \frac{\mu_i c_i}{4\pi^2} \beta_i \sum_{n=1}^{\infty} \frac{(\sinh^2 \zeta_i - \zeta_i^2) B_i^{2n}}{n\lambda \left[\frac{(\sinh^2 \zeta_i - \zeta_i^2) \cdot (1 - \nu_{\langle M \rangle})}{\mu_{\langle M \rangle}} + \frac{(\sinh \zeta_i \cosh \zeta_i - \zeta_i) \cdot (1 - \nu_{\langle MO_x \rangle})}{\mu_{\langle MO_x \rangle}} \right]} \quad (i=1,2), \quad (10a)$$

with

$$\zeta_i = \frac{2\pi n}{d_i} h_{\langle MO_x \rangle}. \quad (10b)$$

The APPR approach is a useful approximation for finite overgrowths, but underestimates the strain energy associated with misfit dislocations in the monolayer regime.¹⁸

5. The Ball approach

In the approach by Ball, which is also based on the theoretical concepts proposed by Frank and van der Merwe,^{17,23} a parabolic representation of the interfacial potential energy is used to arrive at an improved description for the disregistry of the atoms at the interface for the case of an *ultrathin* overgrowth (up to only a few atom layers; treated as a “monolayer” of thickness $h_{\langle MO_x \rangle}$) on a semi-infinite substrate (see Table I). In the BALL approach, the strain gradient perpendicular to the surface/interface plane is neglected, which is a reasonable assumption for ultrathin overgrowths.¹⁸

$$\gamma_{\langle M \rangle - \langle MO_x \rangle}^{\text{dislocation}} = \frac{q_i \mu_i c_i}{d_i 4\pi^2} \left\{ \frac{1}{2} \left[1 + \left(\frac{1}{2} \beta_i^* - 1 \right) B_i^* - \beta_i^* \ln(1 - B_i^{*2}) \right] \right\} \quad (i=1,2), \quad (9b)$$

where the parameters B_i^* and β_i^* are calculated according to Eqs. (7b) and (7c) by replacing d_i by q_i .

The EXTR approach is only a good approximation for films thicker than about ten atom layers, because for smaller film thicknesses the adopted interfacial potential energy density function (as taken from the SIO approach for semi-infinite overgrowths; see Sec. II C 1) differs too much from the actual potential energy density function at the interface between a thin film and a semi-infinite substrate.¹⁸

4. The first approximation (APPR) approach

In the first approximation (APPR) approach,²² a different atom displacement function is derived (i.e., different from that used for the SIO, LDD, and EXTR approaches; e.g., Refs. 18 and 19) to arrive at an improved description for the disregistry of the atoms at the interface for the case of a *finite* overgrowth on a semi-infinite substrate (see Table I).

This results in the following expression for the energy $\gamma_{\langle M \rangle - \langle MO_x \rangle}^{\text{dislocation}}$ of an array of misfit dislocations with a Burgers vector parallel to direction i , per unit area of the semicoherent $\langle M \rangle - \langle MO_x \rangle$ interface, according to the APPR approach¹⁸

In the BALL approach the elastic strain in both the semi-infinite substrate and the ultrathin overgrowth, due to the misfit dislocations, is considered. Further, the interfacial modulus μ_i [see Eq. (6e) in Sec. II C 1] is modified (symbol: μ_i') to approximately correct for errors introduced by the unrealistic parabolic interfacial potential energy density function,¹⁷ i.e.,

$$\mu_i' = \mu_i \frac{8}{\pi^4} [\sqrt{2} + \ln(1 + \sqrt{2})] \quad (i=1,2). \quad (11a)$$

This results in the following expression for the energy $\gamma_{\langle M \rangle - \langle MO_x \rangle}^{\text{dislocation}}$ of an array of misfit dislocations with a Burgers vector parallel to direction i , per unit area of the semicoherent $\langle M \rangle - \langle MO_x \rangle$ interface, according to the BALL approach¹⁷

$${}^i\gamma_{\langle M \rangle - \langle MO_x \rangle}^{\text{dislocation}} = \frac{\mu'_i c_i}{4\pi^2} \cdot \sum_{n=1}^{\infty} \left[n^2 + n/\beta'_i + \frac{1}{2} \cdot \left(\frac{\mu'_i d_i^2}{4\pi\mu_{\langle MO_x \rangle}(1+\nu_{\langle MO_x \rangle})h_{\langle MO_x \rangle}c_i} \right) \right]^{-1} \quad (i=1,2), \quad (11b)$$

with

$$\beta'_i = \frac{2\pi c_i \mu_{\langle M \rangle}}{d_i \mu'_i (1 - \nu_{\langle M \rangle})}. \quad (11c)$$

6. The Volterra (VOLT) approach

In the VOLT approach, which has been extensively used by Matthews,^{24,25} a theoretical treatment on the basis of an adopted interfacial potential energy density function and correspondingly derived atom displacement function (as for the approaches in Secs. II C 1, II C 2, II C 3, II C 4, and II C 5) is no longer employed. Instead, the substrate and the overgrowth are considered as a homogeneous solid with elastic properties equal to the weighted properties of the substrate and the film, i.e., without a real interface as in the aforementioned models. Thereby a variation of the chemical bond strength across the interface is not accounted for and, consequently, the VOLT approach becomes inaccurate for small film thicknesses and/or misfit strains larger than about 10–15%.^{22,25} Since Hooke's law is no longer valid within the dislocation core, in addition to the outer cut-off radius of the strain field of an individual dislocation, an inner cut-off radius has to be defined in the VOLT approach, such that the core energy is effectively included (see below).

This results in the following expression for the energy ${}^i\gamma_{\langle M \rangle - \langle MO_x \rangle}^{\text{dislocation}}$ of an array of misfit dislocations with a Burgers vector parallel to direction i , per unit area of the semicoherent $\langle M \rangle - \langle MO_x \rangle$ interface, according to the VOLT approach²⁵

$${}^i\gamma_{\langle M \rangle - \langle MO_x \rangle}^{\text{dislocation}} = \frac{\lambda |\vec{b}_i|^2}{2\pi d_i} \cdot \ln \left(\frac{R_i}{|\vec{b}_i|} + 1 \right) \quad (i=1,2), \quad (12a)$$

with the outer cut-off radius of the dislocation strain field taken as

$$R_i = \begin{cases} \frac{d_i}{2}, & h_{\langle MO_x \rangle} \geq \frac{d_i}{2} \\ h_{\langle MO_x \rangle}; & h_{\langle MO_x \rangle} \leq \frac{d_i}{2} \end{cases} \quad (i=1,2). \quad (12b)$$

The absolute of the Burgers vector, i.e., $|\vec{b}_i|$, in the logarithmic term of Eq. (12a) is taken as an approximate for the inner cut-off radius of the dislocation strain field. The energy of the associated dislocation core is taken into account by adjustment (i.e., a decreasing) of the inner cut-off radius of the dislocation strain field [as approximated here by the empirical summand one in the logarithmic term of Eq. (12a); see Ref. 25]. As reflected by Eq. (12a), imperfect misfit dislocations (i.e., with realistic Burgers vectors inclined to the

interface or with mixed edge-screw character, as observed from experiment) can be considered in the calculation of the misfit-dislocation energy according to the Volterra (VOLT) approach (see Table I). If the actual Burgers vector for the system under study is not known, its absolute value can be estimated by the lattice spacing of the reference lattice $|\vec{b}_i| \approx c_i$ [see Eq. (6c)].

D. Minimization of $\gamma_{\langle M \rangle - \langle MO_x \rangle}$; numerical procedure

Since the energy contributions due to residual homogeneous strain and misfit dislocations in the crystalline oxide film are assigned to the interface energy $\gamma_{\langle M \rangle - \langle MO_x \rangle}$, instead of to the bulk energy of the film [see Eq. (1) in Sec. II A], it follows that a minimum in the total Gibbs free energy of the crystalline cell [thermodynamic equilibrium; see Fig. 1(b)] is attained if $\gamma_{\langle M \rangle - \langle MO_x \rangle}$ is at its minimum value.²⁶ To determine the minimum value of $\gamma_{\langle M \rangle - \langle MO_x \rangle}$ the residual strain affected lattice spacings ${}^1\bar{a}_{\langle MO_x \rangle}$ and ${}^2\bar{a}_{\langle MO_x \rangle}$ of the crystalline $\langle MO_x \rangle$ film are solved simultaneously by minimization of $\gamma_{\langle M \rangle - \langle MO_x \rangle}$ with respect to the residual homogeneous strain in the film for a given oxide-film thickness, $h_{\langle MO_x \rangle}$, and growth temperature, T , i.e.

$$\frac{\partial \gamma_{\langle M \rangle - \langle MO_x \rangle}}{\partial \bar{\epsilon}_{ij}} = 0, \quad (13)$$

where $\bar{\epsilon}_{ij}$ is the residual strain tensor [see Eq. (5b) in Sec. II B]. The boundary conditions for the minimization are absence of in-plane shear strain in the $\langle \text{Cr} \rangle - \langle \text{Cr}_2\text{O}_3 \rangle$ interface plane (i.e., $\bar{\epsilon}_{12}=0$), as well as absence of stress perpendicular to the interface plane (i.e., $\sigma_{13}=\sigma_{23}=\sigma_{33}=0$). The unstrained initial lattice spacings ${}^1a_{\langle MO_x \rangle}$ and ${}^2a_{\langle MO_x \rangle}$ are used as starting estimates for ${}^1\bar{a}_{\langle MO_x \rangle}$ and ${}^2\bar{a}_{\langle MO_x \rangle}$. The minimization has been performed by adopting the Nelder-Mead simplex method as implemented in Matlab.²⁷

E. General remarks about the misfit-dislocation energy

The dislocation density in a thin film system, as observed from experiment, is generally lower than the value calculated theoretically (i.e., according to one of the equilibrium models discussed in Secs. II C 1, II C 2, II C 3, II C 4, II C 5, and II C 6). This is mainly because kinetic constraints as illustrated by the occurring activation energies for generation and movement of dislocations due to the Peierl's force (e.g., Ref. 24) and the formation of stacking faults and/or surface steps (which can accompany the introduction of misfit dislocations) are not accounted for in the equilibrium models.²¹ Also, in practice, for the system under study, suitable glide systems may lack (thereby prohibiting the built-in and movement of dislocations) and/or a growth mode deviating from ideal layer-by-layer growth (e.g., islands or islands-by-layer growth) may occur. If the actual oxide growth mode deviates from pure layer-by-layer growth, additional growth strain may be relaxed at the edges of oxide islands, as well as by the existence of grain boundaries between adjacent oxide domains.

TABLE II. Unstrained lattice parameters, \tilde{a}^0 and \tilde{c}^0 , and molar volumes, V , at $T_0=298$ K of $\langle\text{Cr}\rangle$ and $\langle\text{Cr}_2\text{O}_3\rangle$. The unstrained lattice parameters and the corresponding molar volumes at a given growth temperature were calculated using the linear thermal expansion coefficient as defined by $\alpha(T)=\alpha_A+\alpha_B T+\alpha_C T^2$.

Phase	Symbol	Value	Unit	Reference	Remark
$\langle\text{Cr}\rangle$	$\tilde{a}_{\langle\text{Cr}\rangle}^0$	2.8849×10^{-10}	m	28	
$\langle\text{Cr}_2\text{O}_3\rangle$	$\tilde{a}_{\langle\text{Cr}_2\text{O}_3\rangle}^0$	4.9573×10^{-10}	m	28	
	$\tilde{c}_{\langle\text{Cr}_2\text{O}_3\rangle}^0$	13.5923×10^{-10}	m	28	
$\langle\text{Cr}\rangle$	α_A	9.983×10^{-7}	K^{-1}	36	for $T < 795$ K
	α_B	2.153×10^{-8}	K^{-2}		
	α_C	-1.152×10^{-11}	K^{-3}		
$\langle\text{Cr}\rangle$	α_A	1.097×10^{-5}	K^{-1}	36	for $T > 795$ K
	α_B	-3.402×10^{-9}	K^{-2}		
	α_C	4.089×10^{-12}	K^{-3}		
$\{\text{Cr}_2\text{O}_3\}$	α_A	1.038×10^{-5}	K^{-1}	37	Data for polycrystalline Cr_2O_3
	α_B	-6.244×10^{-9}	K^{-2}		
	α_C	3.186×10^{-12}	K^{-3}		
$\langle\text{Cr}_2\text{O}_3\rangle$	α_A	1.376×10^{-5}	K^{-1}	37	Along the a -axis
	α_B	-1.200×10^{-9}	K^{-2}		
	α_C	1.628×10^{-12}	K^{-3}		
$\langle\text{Cr}_2\text{O}_3\rangle$	α_A	3.785×10^{-6}	K^{-1}	37	Along the c -axis
	α_B	4.758×10^{-8}	K^{-2}		
	α_C	-1.377×10^{-12}	K^{-3}		
$\{\text{Cr}_2\text{O}_3\}$	$V_{\{\text{Cr}_2\text{O}_3\}}^0$	3.160×10^{-5}	$\text{m}^3 \text{mol}^{-1}$	31	Estimated
$\langle\text{Cr}_2\text{O}_3\rangle$	$V_{\langle\text{Cr}_2\text{O}_3\rangle}^0$	2.903×10^{-5}	$\text{m}^3 \text{mol}^{-1}$	28	

III. ENERGETICS OF CHROMIUM-OXIDE FILMS ON CHROMIUM SUBSTRATES

The thermodynamic model presented in Sec. II is applied here to the case of a thin Cr_2O_3 film of variable, uniform thickness (“overgrowth”) on the $\{110\}$, $\{100\}$, and $\{111\}$ crystallographic faces of a single-crystalline (body centered cubic) Cr substrate, $\langle\text{Cr}\rangle$, for growth temperatures in the range of 298 to 1000 K. An amorphous nature of the Cr_2O_3 film, further denoted as $\{\text{Cr}_2\text{O}_3\}$, competes with a crystalline α - Cr_2O_3 (trigonal, corundum crystal structure; see, e.g., Ref. 28) nature of the film, further designated as $\langle\text{Cr}_2\text{O}_3\rangle$, whether or not containing misfit dislocations.

To calculate the total Gibbs free energies of the amorphous $\{\text{Cr}_2\text{O}_3\}$ and crystalline $\langle\text{Cr}_2\text{O}_3\rangle$ cells (see Fig. 1 and Sec. IV), first the corresponding bulk, surface and interfacial energy contributions [see Eq. (1) in Sec. II A] have to be determined (see Secs. III A–III C, respectively). The crystalline-crystalline $\langle\text{Cr}\rangle$ - $\langle\text{Cr}_2\text{O}_3\rangle$ interfacial energy contribution has been calculated according to the approach presented in this paper (Sec. II B) involving different estimations of the misfit-dislocation energy contributions, $i \gamma_{\langle\text{Cr}\rangle\langle\text{Cr}_2\text{O}_3\rangle}^{\text{dislocation}}$, to the total $\langle\text{Cr}\rangle$ - $\langle\text{Cr}_2\text{O}_3\rangle$ interface energy (see Sec. II C), made by employing the numerical procedure presented in Sec. II D. The corresponding bulk and surface energy contributions of the $\{\text{Cr}_2\text{O}_3\}$ and $\langle\text{Cr}_2\text{O}_3\rangle$ cells (Secs. III A and III B, respectively), as well as the crystalline-amorphous $\langle\text{Cr}\rangle$ - $\{\text{Cr}_2\text{O}_3\}$ interfacial energy contribution (Sec. III C), were calculated according to the procedure described detailedly in Ref. 1.

A. Bulk Gibbs energies of the $\{\text{Cr}_2\text{O}_3\}$ and $\langle\text{Cr}_2\text{O}_3\rangle$ cells

The bulk Gibbs energies of formation, $\Delta G_{\{\text{Cr}_2\text{O}_3\}}^f$ and $\Delta G_{\langle\text{Cr}_2\text{O}_3\rangle}^f$, of $\{\text{Cr}_2\text{O}_3\}$ and $\langle\text{Cr}_2\text{O}_3\rangle$, respectively, have been taken from Ref. 29. The bulk Gibbs energy of formation of liquid Cr_2O_3 below the glass-transition temperature²⁹ has been adopted as an approximate for the value of $\Delta G_{\{\text{Cr}_2\text{O}_3\}}^f$ for amorphous $\{\text{Cr}_2\text{O}_3\}$, treated as a configurationally frozen liquid (see Ref. 1). The corresponding molar volumes of $\{\text{Cr}_2\text{O}_3\}$ and $\langle\text{Cr}_2\text{O}_3\rangle$ at $T_0=298$ K are shown in Table II.

The calculated difference in bulk Gibbs energy contribution [see Eq. (1)], $h_{\{\text{Cr}_2\text{O}_3\}} \cdot (\Delta G_{\{\text{Cr}_2\text{O}_3\}}^f - \Delta G_{\langle\text{Cr}_2\text{O}_3\rangle}^f) / V_{\{\text{Cr}_2\text{O}_3\}}$, per unit area of the $\langle\text{Cr}\rangle$ - $\{\text{Cr}_2\text{O}_3\}$ interface, has been plotted in Fig. 3 as a function of the thickness, $h_{\{\text{Cr}_2\text{O}_3\}}$, of the $\{\text{Cr}_2\text{O}_3\}$ cell for both $T_0=298$ K and $T=1000$ K. Obviously, if only the bulk Gibbs energies of the competing cells are considered, the crystalline $\langle\text{Cr}_2\text{O}_3\rangle$ cell is thermodynamically preferred. The bulk Gibbs energy difference between the competing cells decreases with increasing temperature (equal values of ΔG^f occur at the $\langle\text{Cr}_2\text{O}_3\rangle$ melting point).

B. Surface energies of the $\{\text{Cr}_2\text{O}_3\}$ and $\langle\text{Cr}_2\text{O}_3\rangle$ cells

For the calculation of the $\langle\text{Cr}\rangle$ - $\langle\text{Cr}_2\text{O}_3\rangle$ interface (Sec. III C) and surface energy contributions, the following orientation relationship between the $\{110\}$, $\{100\}$, and $\{111\}$ faces of the body centered cubic (bcc) $\langle\text{Cr}\rangle$ substrate and the

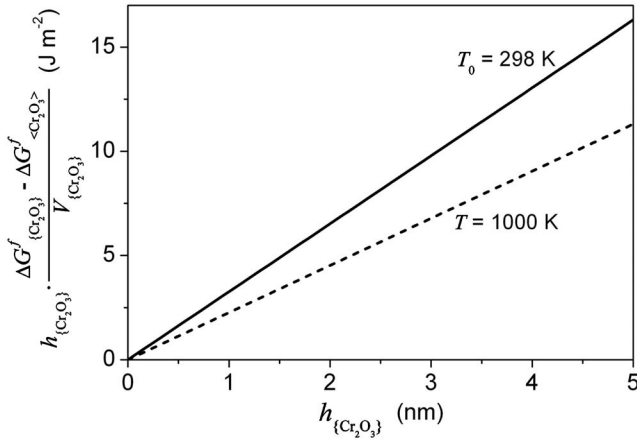


FIG. 3. Difference in bulk Gibbs energy of formation of the amorphous $\{Cr_2O_3\}$ and the crystalline $\langle Cr_2O_3 \rangle$ cells, per unit area of the $\langle Cr \rangle$ - $\{Cr_2O_3\}$ interface [see Eq. (1) in Sec. II A and see Fig. 1], as function of the thickness, $h_{\langle Cr_2O_3 \rangle}$, of the amorphous $\{Cr_2O_3\}$ overgrowth at $T_0=298$ K and $T=1000$ K.

trigonal (corundum) $\langle Cr_2O_3 \rangle$ film has been adopted: $(110)_{\langle Cr \rangle} \parallel (0001)_{\langle Cr_2O_3 \rangle}$ and $[1\bar{1}0]_{\langle Cr \rangle} \parallel [01\bar{1}0]_{\langle Cr_2O_3 \rangle}$ (as experimentally observed for thin crystalline Cr_2O_3 films grown on $\{110\}$ and $\{111\}$ faces of single-crystalline Cr substrates by thermal oxidation^{7,12,30}). Consequently, the $Cr_2O_3(0001)$, $Cr_2O_3(\bar{1}\bar{1}26)$, and $Cr_2O_3(\bar{1}104)$ crystallographic planes constitute the surfaces of the crystalline $\langle Cr_2O_3 \rangle$ overgrowths on the Cr(110), Cr(100), and Cr(111) substrates, respectively.

The values adopted for the surface energies of the $\{Cr_2O_3\}$ and $\langle Cr_2O_3 \rangle$ cells (and their temperature dependence) have been gathered in Table III. The employed temperature dependence of the $\langle Cr_2O_3 \rangle$ surface energies (Table III) represents an empirical estimate as obtained from the averaged temperature dependence for various crystalline oxide surfaces.^{31,32} The employed temperature dependence of the $\{Cr_2O_3\}$ surface energy (Table III) represents an empirical estimate as obtained from the averaged temperature dependence of various liquid and amorphous oxides.^{31,33}

The literature value for the surface energy of the relaxed

$Cr_2O_3(0001)$ surface has been obtained by atomistic lattice simulations performed at $T=0$ K.⁴ No literature values for the $Cr_2O_3(\bar{1}\bar{1}26)$ and $Cr_2O_3(\bar{1}104)$ surface energies could be found. Therefore, literature values for the energies of the relaxed $Cr_2O_3\{0001\}$ and $Cr_2O_3\{11\bar{2}0\}$ surfaces³⁴ have been employed to estimate the surface energy of the $Cr_2O_3(\bar{1}\bar{1}26)$ surface at $T=0$ K, by conceiving the stepped $Cr_2O_3(\bar{1}\bar{1}26)$ surface as constituted of $Cr_2O_3(0001)$ and $Cr_2O_3(\bar{1}\bar{1}20)$ crystallographic planes (facets). Similarly, the energy of the stepped $Cr_2O_3(\bar{1}104)$ surface at $T=0$ K has been estimated from literature values for the relaxed $Cr_2O_3\{0001\}$ and $Cr_2O_3\{10\bar{1}0\}$ surfaces. The thus obtained surface energies of the concerned crystalline $\langle Cr_2O_3 \rangle$ cells obey $\gamma_{\langle Cr_2O_3(0001) \rangle - vac} < \gamma_{\langle Cr_2O_3(\bar{1}\bar{1}26) \rangle - vac} < \gamma_{\langle Cr_2O_3(\bar{1}104) \rangle - vac}$ (see Table III).

The surface energy at $T=0$ K of the amorphous $\{Cr_2O_3\}$ cell (on all three crystallographic faces of the $\langle Cr \rangle$ substrate) is approximated to be $\frac{3}{4}$ of the corresponding, most densely packed crystalline oxide surface, i.e., the $Cr_2O_3(0001)$ surface (see Refs. 31 and 35).

The calculated difference in surface energy, $\gamma_{\langle Cr_2O_3 \rangle - vac} - \chi \cdot \gamma_{\langle Cr_2O_3 \rangle - vac}$ [cf. Eq. (1)], per unit area of the $\{Cr_2O_3\}$ surface, has been plotted in Fig. 4 as function of T for oxide growth on the Cr $\{110\}$, Cr $\{100\}$, and Cr $\{111\}$ substrates for $h_{\langle Cr_2O_3 \rangle}=2$ nm. The surface energy difference decreases slightly with increasing $h_{\langle Cr_2O_3 \rangle}$ (up to about 1 nm thickness), as a consequence of the concurrent change of the surface area ratio, χ of the competing cells in the mixed regime [see Eq. (2) in Sec. II A]. Therefore, the results in Fig. 4 have been given for a specific thickness within the plastic regime (i.e., $h_{\langle Cr_2O_3 \rangle}=2$ nm). It follows from Fig. 4 that the surface energy of the amorphous $\{Cr_2O_3\}$ cell is in all cases lower than that of the corresponding crystalline $\langle Cr_2O_3 \rangle$ cell, which is a factor contributing to a possible stabilization of the amorphous $\{Cr_2O_3\}$ cell (see Sec. IV). The surface energy difference is least negative for the most densely packed $Cr_2O_3(0001)$ surface. Further, the surface energy difference increases with increasing T due to the stronger (negative) temperature dependence of the crystalline surface energy.

TABLE III. Surface energies, $\gamma_{\langle Cr \rangle - vac}$, $\gamma_{\langle Cr_2O_3 \rangle - vac}$, and $\gamma_{\{Cr_2O_3\} - vac}$, at $T_0=298$ K and their temperature dependence, $\partial\gamma_{\text{phase-vac}}/\partial T$, for the differently oriented $\langle Cr \rangle$ substrates and the $\{Cr_2O_3\}$ and $\langle Cr_2O_3 \rangle$ cells of the corresponding overgrowths (see Fig. 1), as adopted in the model calculations.

Phase	Crystallographic surface plane	$\gamma_{\text{phase-vac}}$ (J m ⁻²)	$\partial\gamma_{\text{phase-vac}}/\partial T$ (J m ⁻² K ⁻¹)	Reference
$\langle Cr \rangle$	$\{110\}$	2.62	}	-3×10^{-4}
	$\{100\}$	2.24		
	$\{111\}$	2.50		
$\{Cr_2O_3\}$	—	1.21		-1×10^{-4}
$\langle Cr_2O_3 \rangle$	$\{0001\}$	1.61	}	-4×10^{-4}
	$\{\bar{1}\bar{1}26\}$	2.47		
	$\{\bar{1}104\}$	2.57		

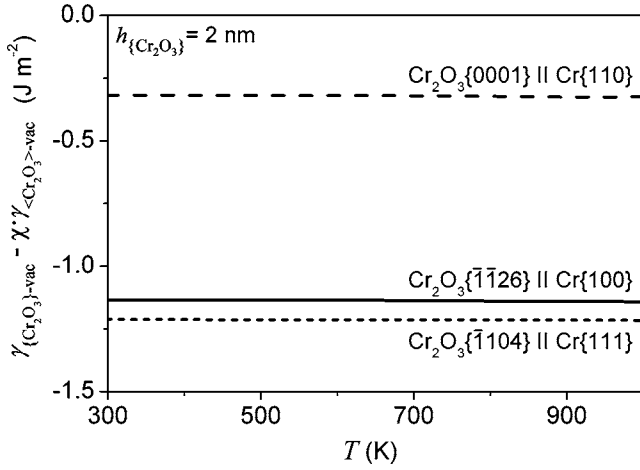


FIG. 4. Surface energy difference, $\gamma_{\{Cr_2O_3\}-vac} - \chi \gamma_{\langle Cr_2O_3 \rangle - vac}$, per unit area of the $\{Cr_2O_3\}$ surface, as function of the growth temperature, T , for the competing amorphous $\{Cr_2O_3\}$ and crystalline $\langle Cr_2O_3 \rangle$ cells on the $\{110\}$, $\{100\}$, and $\{111\}$ faces of the $\langle Cr \rangle$ substrate [and for a thickness of the $\{Cr_2O_3\}$ overgrowth of $h_{\{Cr_2O_3\}} = 2$ nm; see Eq. (1) and Fig. 1]. The surface plane of the $\langle Cr_2O_3 \rangle$ overgrowth corresponds with the $Cr_2O_3(0001)$, the $Cr_2O_3(\bar{1}\bar{1}26)$ and the $Cr_2O_3(\bar{1}\bar{1}04)$ crystallographic faces, respectively.

C. Interfacial energies of the $\{Cr_2O_3\}$ and $\langle Cr_2O_3 \rangle$ cells

1. The interface energy of the crystalline-amorphous $\langle Cr \rangle$ - $\{Cr_2O_3\}$ interface

The interface energy, $\gamma_{\langle Cr \rangle - \{Cr_2O_3\}}$, of the crystalline-amorphous $\langle Cr \rangle$ - $\{Cr_2O_3\}$ interface is the resultant of the interaction, entropy and enthalpy contributions [cf. Eq. (3)]. Values for the interaction, entropy and enthalpy contributions have been calculated as function of the growth temperature and oxide-film thickness according to the procedure outlined in Ref. 1, employing the data gathered in Table II and Refs. 1 and 29.

The thus obtained values of $\gamma_{\langle Cr \rangle - \{Cr_2O_3\}}^{interaction}$, $\gamma_{\langle Cr \rangle - \{Cr_2O_3\}}^{entropy}$, $\gamma_{\langle Cr \rangle - \{Cr_2O_3\}}^{enthalpy}$ and of the resultant $\gamma_{\langle Cr \rangle - \{Cr_2O_3\}}$ for amorphous oxide growth on the $Cr\{110\}$, $Cr\{100\}$, and $Cr\{111\}$ substrates have been given in Table IV for various growth temperatures. It follows that the (negative) interaction contribution is the largest energy contribution, overruling the minor (positive) entropy and enthalpy contributions, resulting in a nega-

tive value for the interface energy, $\gamma_{\langle Cr \rangle - \{Cr_2O_3\}}$. The enthalpy contribution depends on the orientation of the $\langle Cr \rangle$ substrate and is larger for a more densely packed substrate surface (approximately independent of the growth temperature). The resultant interface energy, $\gamma_{\langle Cr \rangle - \{Cr_2O_3\}}$, only slightly increases (i.e., becomes less negative) with temperature, due to the increase of the interaction (via the temperature dependence of the lattice spacings) and entropy contributions.

2. The interface energy of the crystalline-crystalline $\langle Cr \rangle$ - $\langle Cr_2O_3 \rangle$ interface

The interface energy, $\gamma_{\langle Cr \rangle - \langle Cr_2O_3 \rangle}$, of the crystalline-crystalline $\langle Cr \rangle$ - $\langle Cr_2O_3 \rangle$ interface is the resultant of the interaction contribution and the mismatch contribution [Eq. (4a)], which latter is further subdivided into a contribution due to the presence of residual strain in the $\langle Cr_2O_3 \rangle$ overgrowth and a contribution due to the misfit dislocations at the $\langle Cr \rangle$ - $\langle Cr_2O_3 \rangle$ interface [Eq. (4b)]. Values for the interaction and mismatch contributions have been calculated as function of the growth temperature and oxide-film thickness according to the numerical procedure outlined in Sec. II D, employing Eqs. (4c)–(4e) and (5b) and the data reported in Tables II, III, V, and VI, and Refs. 1 and 29. The calculations have been performed for each of the different expressions of the misfit-dislocation energy contribution, $\gamma_{\langle Cr \rangle - \langle Cr_2O_3 \rangle}^{dislocation}$, presented in Secs. II C 2, II C 3, II C 4, II C 5, and II C 6. The thus obtained resultant interfacial energies, $\gamma_{\langle Cr \rangle - \langle Cr_2O_3 \rangle}$, have been plotted in Figs. 5(a)–5(c) as a function of the crystalline oxide-film thickness, $h_{\langle Cr_2O_3 \rangle}$, for a $\langle Cr_2O_3 \rangle$ overgrowth on the $Cr\{110\}$, $Cr\{100\}$, and $Cr\{111\}$ substrates, respectively. Additionally, values of $\gamma_{\langle Cr \rangle - \langle Cr_2O_3 \rangle}$ have been plotted in Fig. 5 for the two limiting cases that (i) all lattice mismatch is fully accommodated by either elastic strain (i.e., only the elastic regime is considered; as calculated according to Ref. 1) or (ii) all lattice mismatch is fully accommodated by misfit dislocations (i.e., only the plastic regime is considered; as calculated using the SIO approach discussed in Sec. II C 1). The equivalent thickness in the number of oxide monolayers (see abscissa at the top of Fig. 5) has been obtained by taking the approximate thickness of one oxide monolayer equal to $\frac{1}{6}c_{\langle Cr_2O_3 \rangle}^0 \cong 0.23$ nm.

To discuss these results it is first noted that a much larger initial lattice mismatch, f [see Eq. (5a)], exists along the

TABLE IV. Values of the interaction, $\gamma_{\langle Cr \rangle - \{Cr_2O_3\}}^{interaction}$, entropy, $\gamma_{\langle Cr \rangle - \{Cr_2O_3\}}^{entropy}$, and enthalpy, $\gamma_{\langle Cr \rangle - \{Cr_2O_3\}}^{enthalpy}$, energy contributions to the resultant $\langle Cr \rangle$ - $\{Cr_2O_3\}$ interfacial energy, $\gamma_{\langle Cr \rangle - \{Cr_2O_3\}}$, for the overgrowth of the amorphous $\{Cr_2O_3\}$ cell [see Fig. 1(a)] on the differently oriented $\langle Cr \rangle$ substrates for various growth temperatures, T , and film thicknesses, $h_{\{Cr_2O_3\}}$. All data have been calculated according to the procedure outlined in Ref. 1, employing the data reported in Table II and Refs. 1 and 29 (see also Sec. II B).

T (K)	$\gamma_{\langle Cr \rangle - \{Cr_2O_3\}}^{interaction}$ ($J m^{-2}$)	$\gamma_{\langle Cr \rangle - \{Cr_2O_3\}}^{entropy}$ ($J m^{-2}$)	$\gamma_{\langle Cr \rangle - \{Cr_2O_3\}}^{enthalpy}$ ($J m^{-2}$)			$\gamma_{\langle Cr \rangle - \{Cr_2O_3\}}$ ($J m^{-2}$)		
			{110}	{100}	{111}	{110}	{100}	{111}
298	-1.73	0.07	0.25	0.17	0.10	-1.42	-1.49	-1.56
500	-1.71	0.11	0.24	0.17	0.10	-1.35	-1.50	-1.42
1000	-1.56	0.22	0.24	0.17	0.10	-1.10	-1.17	-1.24

TABLE V. Single-crystal elastic compliances, C_{ij} , shear modulus, μ , and Poisson constants, ν , of $\langle\text{Cr}\rangle$ and $\langle\text{Cr}_2\text{O}_3\rangle$ as taken from Refs. 42 and 43. The abbreviation “n.a.” stands for “not available” (to indicate that no literature values or estimates are available).

Symbol	Unit	$\langle\text{Cr}\rangle$	$\langle\text{Cr}_2\text{O}_3\rangle$
C_{11}	Pa	355.0×10^9	374×10^9
C_{12}	Pa	46.0×10^9	148×10^9
C_{13}	Pa	C_{12}	175×10^9
C_{14}	Pa	0	-19×10^9
C_{33}	Pa	C_{11}	362×10^9
C_{44}	Pa	104.0×10^9	159×10^9
$\partial C_{11}/\partial T$	Pa K ⁻¹	-2.0×10^7	n.a.
$\partial C_{22}/\partial T$	Pa K ⁻¹	6.0×10^7	n.a.
$\partial C_{44}/\partial T$	Pa K ⁻¹	-1.0×10^7	n.a.
μ	Pa	120.4×10^9	187×10^9
ν	—	0.193	0.192
$\partial\mu/\partial T$	Pa K ⁻¹	-1.7×10^7	n.a.
$\partial\nu/\partial T$	K ⁻¹	6×10^{-5}	n.a.

defined direction 1 (i.e., $f_1 \sim -18\%$ to -14%) than along the perpendicular direction 2 (i.e., $f_2 \sim -3\%$ to $+1\%$) within the $\langle\text{Cr}\rangle$ - $\langle\text{Cr}_2\text{O}_3\rangle$ interface plane (see Table VI). Consequently, a large anisotropic strain resides within the $\langle\text{Cr}_2\text{O}_3\rangle$ film at the onset of growth: a large compressive stress along direction 1 and either a small tensile or small compressive stress along direction 2. Since the thermal expansion coefficients of $\langle\text{Cr}\rangle$ and $\langle\text{Cr}_2\text{O}_3\rangle$ are of the same order of magnitude (Table II), the initial lattice mismatch values f_1 and f_2 only slightly change (i.e., increase with about 0.2%) with increasing temperature up to 1000 K.

Because the initial lattice mismatch for the investigated Cr-Cr₂O₃ system is large, the assumption that all mismatch is accommodated fully elastically leads to a severe overestimation of the interface energy, $\gamma_{\langle\text{Cr}\rangle-\langle\text{Cr}_2\text{O}_3\rangle}$, beyond an oxide-film thicknesses of one oxide monolayer (see bold dashed

lines in Fig. 5). On the other hand, if it is assumed that all lattice mismatch is fully accommodated by plastic deformation, the resulting value of $\gamma_{\langle\text{Cr}\rangle-\langle\text{Cr}_2\text{O}_3\rangle}$ may lead to large overestimation of the interface energy within the submonolayer thickness regime (see bold solid lines in Fig. 5).

As follows from Fig. 5, both the VOLT approach and the LDD approach yield unrealistic results in the mixed and plastic regimes: interface energy values much larger than the limiting interfacial energy value for pure plastic accommodation. This is due to the large initial mismatch, f_1 , in direction 1 within the $\langle\text{Cr}\rangle$ - $\langle\text{Cr}_2\text{O}_3\rangle$ interface planes (see above) which results in a relatively small dislocation distance, d_1 , along this direction (even at the onset of growth). Consequently, the main assumption $c_i^2/d_i^2 \approx 0$ made in the LDD approach (see Sec. II C 2) no longer holds. The VOLT approach does not account for a change of the chemical bond strength across the interface (Sec. II C 6), as is required, in particular, for thin overgrowths with high dislocation densities (as considered here),^{21,25} and hence the results of the VOLT approach are unrealistic for the case considered (i.e., it is more useful for interfaces between materials which are chemically very alike, such as specific metal/metal interfaces).

The other approaches (i.e., the EXTR, BALL, and APPR approaches) used to estimate the misfit-dislocation energy contribution result in a value of $\gamma_{\langle\text{Cr}\rangle-\langle\text{Cr}_2\text{O}_3\rangle}$ that is generally lower than the corresponding limiting values for the elastic and plastic regimes (Fig. 5). Only for the $\langle\text{Cr}_2\text{O}_3\rangle$ overgrowths with $h_{\langle\text{Cr}_2\text{O}_3\rangle} > 1$ nm on the Cr {111} substrate [Fig. 5(c)], the $\langle\text{Cr}\rangle$ - $\langle\text{Cr}_2\text{O}_3\rangle$ interfacial energy as calculated using the BALL and (especially) the APPR approach slightly exceeds the corresponding limiting value for the plastic regime. This slight, “apparent” overestimation of the value of $\gamma_{\langle\text{Cr}\rangle-\langle\text{Cr}_2\text{O}_3\rangle}$ is due to the different interfacial potential energy density functions employed in the APPR and BALL approaches (as adopted for overgrowths of finite thickness; see Secs. II C 4 and II C 5, respectively).

The interfacial energies as calculated using the EXTR approach are considerably lower than those calculated using

TABLE VI. The directions 1 and 2 in the $\langle\text{Cr}\rangle$ - $\langle\text{Cr}_2\text{O}_3\rangle$ interface plane and the unstrained lattice spacings in the same directions of the $\langle\text{Cr}\rangle$ substrate, $^1a_{\langle\text{Cr}\rangle}$ and $^2a_{\langle\text{Cr}\rangle}$, and of the $\langle\text{Cr}_2\text{O}_3\rangle$ overgrowth, $^1a_{\langle\text{Cr}_2\text{O}_3\rangle}$ and $^2a_{\langle\text{Cr}_2\text{O}_3\rangle}$, at $T_0 = 298$ K for the $\langle\text{Cr}_2\text{O}_3\rangle$ overgrowth on the {110}, {100}, and {111} crystallographic faces of the $\langle\text{Cr}\rangle$ substrate. The corresponding *initial* lattice mismatches f_1 and f_2 along the perpendicular directions 1 and 2 [see Eq. (5a) in Sec. II B] have also been indicated.

Symbol	On Cr{110}	On Cr{100}	On Cr{111}
Direction 1	$[1\bar{1}0]_{\langle\text{Cr}\rangle} \parallel [11\bar{2}0]_{\langle\text{Cr}_2\text{O}_3\rangle}$	$[1\bar{1}0]_{\langle\text{Cr}\rangle} \parallel [11\bar{2}0]_{\langle\text{Cr}_2\text{O}_3\rangle}$	$[1\bar{1}0]_{\langle\text{Cr}\rangle} \parallel [11\bar{2}0]_{\langle\text{Cr}_2\text{O}_3\rangle}$
Direction 2	$[001]_{\langle\text{Cr}\rangle} \parallel [1\bar{1}00]_{\langle\text{Cr}_2\text{O}_3\rangle}$	$[001]_{\langle\text{Cr}\rangle} \parallel [1\bar{1}00]_{\langle\text{Cr}_2\text{O}_3\rangle}$	$[\bar{1}\bar{1}2]_{\langle\text{Cr}\rangle} \parallel [1\bar{1}01]_{\langle\text{Cr}_2\text{O}_3\rangle}$
$^1a_{\langle\text{Cr}\rangle}$	$\sqrt{2}\tilde{a}_{\langle\text{Cr}\rangle}$	$2\tilde{a}_{\langle\text{Cr}\rangle}$	$\sqrt{2}\tilde{a}_{\langle\text{Cr}\rangle}$
$^1a_{\langle\text{Cr}_2\text{O}_3\rangle}$	$\tilde{a}_{\langle\text{Cr}_2\text{O}_3\rangle}$	$\frac{1}{3}\sqrt{9\tilde{a}_{\langle\text{Cr}_2\text{O}_3\rangle}^2 + \tilde{c}_{\langle\text{Cr}_2\text{O}_3\rangle}^2}$	$\tilde{a}_{\langle\text{Cr}_2\text{O}_3\rangle}$
$^2a_{\langle\text{Cr}\rangle}$	$3\tilde{a}_{\langle\text{Cr}\rangle}$	$3\tilde{a}_{\langle\text{Cr}\rangle}$	$3\sqrt{3}/2\tilde{a}_{\langle\text{Cr}\rangle}$
$^2a_{\langle\text{Cr}_2\text{O}_3\rangle}$	$\sqrt{3}\tilde{a}_{\langle\text{Cr}_2\text{O}_3\rangle}$	$\sqrt{3}\tilde{a}_{\langle\text{Cr}_2\text{O}_3\rangle}$	$\frac{1}{2}\sqrt{12\tilde{a}_{\langle\text{Cr}_2\text{O}_3\rangle}^2 + \tilde{c}_{\langle\text{Cr}_2\text{O}_3\rangle}^2}$
f_1 (%)	-17.7	-14.1	-17.7
f_2 (%)	0.8	0.8	-3.2

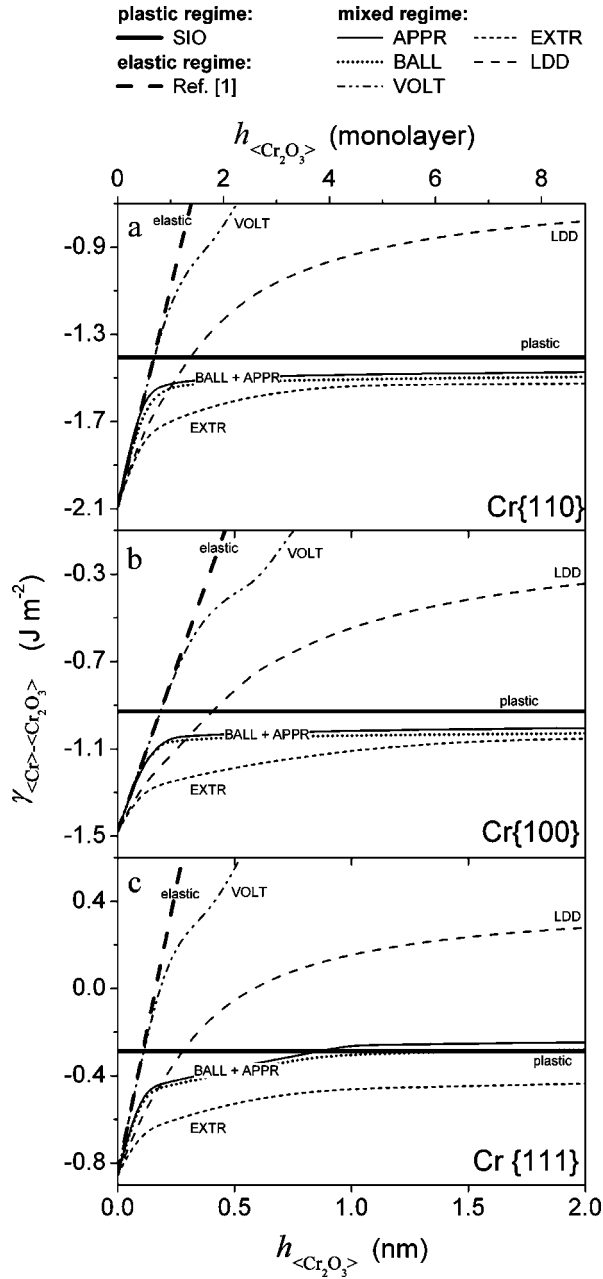


FIG. 5. Crystalline-crystalline interface energy, $\gamma_{\langle\text{Cr}\rangle-\langle\text{Cr}_2\text{O}_3\rangle}$, as function of the oxide-film thickness $h_{\langle\text{Cr}_2\text{O}_3\rangle}$ at $T_0=298$ K, for the $\langle\text{Cr}_2\text{O}_3\rangle$ overgrowth on the (a) Cr{110}, (b) Cr{100}, and (c) Cr{111} faces of the $\langle\text{Cr}\rangle$ substrate. The bold solid and bold dashed lines correspond to the two limiting cases that all lattice mismatch is fully accommodated by either elastic strain (fully elastic accommodation according to Ref. 1) or misfit dislocations (fully plastic accommodation according to the SIO approach in Sec. II C 1), respectively. All other data correspond to values of $\gamma_{\langle\text{Cr}\rangle-\langle\text{Cr}_2\text{O}_3\rangle}$ in the mixed regime (Fig. 2), as obtained by employing the different indicated approaches for the estimation of the misfit-dislocation energy contribution, $i\gamma_{\langle\text{Cr}\rangle-\langle\text{Cr}_2\text{O}_3\rangle}^{\text{dislocation}}$ (see Secs. II C 2, II C 3, II C 4, II C 5, and II C 6).

the BALL and APPR approach (Fig. 5), which can be attributed to an underestimation of the effective dislocation strain field and the application of an inappropriate interfacial po-

tential energy density function (as derived for infinitely thick overgrowths) within the thin-film regime. The EXTR approach is only valid for $\langle\text{Cr}_2\text{O}_3\rangle$ overgrowths thicker than about ten oxide monolayers.

The values of $\gamma_{\langle\text{Cr}\rangle-\langle\text{Cr}_2\text{O}_3\rangle}$ calculated according to the BALL and APPR approaches, are nearly equal over the entire thickness range considered (i.e., from 0 to 2 nm; see Fig. 5), with the interface energy as obtained using the BALL approach being systematically a little lower, presumably because the strain gradient perpendicular to the surface/interface plane is not accounted for in the BALL approach (which assumption is reasonable only in the monolayer-thickness regime; see Sec. II C 5).

It is therefore concluded that the EXTR, the APPR, and the BALL approaches are especially suitable for thinner overgrowths (see Table I) with the APPR approach having the greatest overall accuracy, in agreement with the findings in Ref. 22. The applicability of the BALL approach is confined to the submonolayer to monolayer thickness regime. The SIO, the LDD, and the VOLT approaches are only suitable for relatively thick overgrowths (see Table I); the VOLT approach being only applicable for interfaces which are chemically very alike (e.g., specific metal/metal systems), the LDD approach being only applicable for small mismatch systems, and the SIO approach being only valid within the plastic regime.

As an outcome of the above discussion, the APPR approach will be employed further to assess the misfit-dislocation energy contribution, $i\gamma_{\langle\text{Cr}\rangle-\langle\text{Cr}_2\text{O}_3\rangle}^{\text{dislocation}}$ in the current model calculations (recognizing that the other approaches can be applicable for larger film thicknesses and/or metal-oxide systems with small initial lattice-mismatch values). The resulting value of $\gamma_{\langle\text{Cr}\rangle-\langle\text{Cr}_2\text{O}_3\rangle}$ (i.e., as calculated using the APPR approach) increases with increasing thickness, $h_{\langle\text{Cr}_2\text{O}_3\rangle}$, initially very fast and approximately linearly within the submonolayer thickness regime, and then increases more gradually within the mixed regime (Fig. 5). Upon approaching the plastic regime (i.e., for thicknesses $h_{\langle\text{Cr}_2\text{O}_3\rangle} > 2$ nm), the interface energy becomes nearly independent of the film thickness, because practically all mismatch strain becomes fully accommodated by misfit dislocations at the $\langle\text{Cr}\rangle-\langle\text{Cr}_2\text{O}_3\rangle$ interface.

Values of the interaction, $\gamma_{\langle\text{Cr}\rangle-\langle\text{Cr}_2\text{O}_3\rangle}^{\text{interaction}}$, and mismatch, $\gamma_{\langle\text{Cr}\rangle-\langle\text{Cr}_2\text{O}_3\rangle}^{\text{mismatch}}$, energy contributions, as calculated using the APPR approach, and the resultant value of the $\langle\text{Cr}\rangle-\langle\text{Cr}_2\text{O}_3\rangle$ interfacial energy, $\gamma_{\langle\text{Cr}\rangle-\langle\text{Cr}_2\text{O}_3\rangle}$, have been gathered in Table VII for crystalline oxide overgrowth on the differently oriented $\langle\text{Cr}\rangle$ substrates at various growth temperatures and for various film thicknesses, $h_{\langle\text{Cr}_2\text{O}_3\rangle}$. The corresponding residual homogeneous strains in the $\langle\text{Cr}_2\text{O}_3\rangle$ overgrowth (i.e., ε_{11} and ε_{22} along the defined directions 1 and 2 within the $\langle\text{Cr}\rangle-\langle\text{Cr}_2\text{O}_3\rangle$ interface plane, respectively; see Table VI) have been plotted in Figs. 6(a)–6(c) as a function of $h_{\langle\text{Cr}_2\text{O}_3\rangle}$ at $T_0=298$ K. Finally, the energy contributions $\gamma_{\langle\text{Cr}\rangle-\langle\text{Cr}_2\text{O}_3\rangle}^{\text{interaction}}$, $\gamma_{\langle\text{Cr}\rangle-\langle\text{Cr}_2\text{O}_3\rangle}^{\text{strain}}$, and $i\gamma_{\langle\text{Cr}\rangle-\langle\text{Cr}_2\text{O}_3\rangle}^{\text{dislocation}}$ ($i=1,2$) to the resultant $\langle\text{Cr}\rangle-\langle\text{Cr}_2\text{O}_3\rangle$ interfacial energy, $\gamma_{\langle\text{Cr}\rangle-\langle\text{Cr}_2\text{O}_3\rangle}$, are shown in Figs. 7(a)–7(c) as a function of $h_{\langle\text{Cr}_2\text{O}_3\rangle}$ at $T_0=298$ K.

TABLE VII. Values of the interaction, $\gamma_{\langle\text{Cr}\rangle-\langle\text{Cr}_2\text{O}_3\rangle}^{\text{interaction}}$, and mismatch, $\gamma_{\langle\text{Cr}\rangle-\langle\text{Cr}_2\text{O}_3\rangle}^{\text{mismatch}}$, energy contributions to the resultant $\langle\text{Cr}\rangle-\langle\text{Cr}_2\text{O}_3\rangle$ interfacial energy, $\gamma_{\langle\text{Cr}\rangle-\langle\text{Cr}_2\text{O}_3\rangle}$, for the overgrowth of the crystalline $\langle\text{Cr}_2\text{O}_3\rangle$ cell [see Fig. 1(b)] on the differently oriented $\langle\text{Cr}\rangle$ substrates for various growth temperatures, T , and film thicknesses, $h_{\langle\text{Cr}_2\text{O}_3\rangle}$, (see Sec. II B). All data have been calculated according to the numerical procedure outlined in Sec. II D, employing Eqs. (4c)–(4e) and (5b) and the data reported in Tables II, III, V, and VI, and Refs. 1 and 29. In the calculations, the APPR approach (Sec. II C 4) has been employed to estimate the misfit-dislocation energy contributions, $\gamma_{\langle\text{Cr}\rangle-\langle\text{Cr}_2\text{O}_3\rangle}^{i, \text{dislocation}}$. See also Fig. 7.

T (K)	$h_{\langle\text{Cr}_2\text{O}_3\rangle}$ (nm)	$\gamma_{\langle\text{Cr}\rangle-\langle\text{Cr}_2\text{O}_3\rangle}^{\text{interaction}}$ ($J m^{-2}$)			$\gamma_{\langle\text{Cr}\rangle-\langle\text{Cr}_2\text{O}_3\rangle}^{\text{mismatch}}$ ($J m^{-2}$)			$\gamma_{\langle\text{Cr}\rangle-\langle\text{Cr}_2\text{O}_3\rangle}$ ($J m^{-2}$)		
		{110}	{100}	{111}	{110}	{100}	{111}	{110}	{100}	{111}
298	1	-1.73	-1.28	-0.68	0.25	0.26	0.42	-1.49	-1.02	-0.26
	3	-1.72	-1.27	-0.68	0.26	0.28	0.44	-1.46	-1.00	-0.24
	5	-1.72	-1.27	-0.68	0.28	0.29	0.45	-1.45	-0.98	-0.23
500	1	-1.71	-1.26	-0.68	0.24	0.25	0.42	-1.47	-1.01	-0.26
	3	-1.70	-1.26	-0.67	0.26	0.27	0.43	-1.45	-0.98	-0.24
	5	-1.70	-1.25	-0.67	0.27	0.29	0.44	-1.43	-0.97	-0.23
1000	1	-1.55	-1.14	-0.62	0.22	0.24	0.39	-1.33	-0.90	-0.23
	3	-1.54	-1.14	-0.61	0.26	0.27	0.41	-1.29	-0.87	-0.20
	5	-1.55	-1.14	-0.61	0.29	0.30	0.42	-1.26	-0.84	-0.20

The film thickness beyond which misfit dislocations are introduced at the $\langle\text{Cr}\rangle-\langle\text{Cr}_2\text{O}_3\rangle$ interface, where upon the homogeneous strain within the $\langle\text{Cr}_2\text{O}_3\rangle$ overgrowth is reduced significantly [see arrows in Figs. 6(b) and 6(c)], strongly depends on the initial lattice mismatch values f_1 and f_2 at the onset of growth (compare Figs. 6 and 7 and Table VI). For the $\langle\text{Cr}_2\text{O}_3\rangle$ overgrowths on the Cr{110} and Cr{111} substrates, a large initial lattice mismatch is present along direction 1 (i.e., $f_1 = -17.7\%$; see Table VI) and, consequently, misfit dislocations are introduced already at the onset of growth along this direction [note the decrease of the *absolute* value of ϵ_{11} with increasing thickness for $h_{\langle\text{Cr}_2\text{O}_3\rangle} > 0$ nm; see Figs. 6(a) and 6(c)]. For the $\langle\text{Cr}_2\text{O}_3\rangle$ overgrowth on the Cr{100} substrate with $f_1 = -14.1\%$, misfit dislocations are introduced in the submonolayer thickness regime [i.e., $h_{\langle\text{Cr}_2\text{O}_3\rangle} < 0.2$ nm; see Fig. 6(b)]. For the $\langle\text{Cr}_2\text{O}_3\rangle$ overgrowths on the Cr{110}, Cr{111}, and Cr{100} substrates in the plastic regime (i.e., if all lattice mismatch is fully accommodated by only misfit dislocations), dislocation distances along direction 1 of five, five and seven lattice spacings \bar{c}_1 have been obtained from the model calculations, respectively.

For the $\langle\text{Cr}_2\text{O}_3\rangle$ overgrowth on the Cr{111} substrate, an additional, considerable (compressive) initial strain of $\epsilon_{22} = f_2 = -3.2\%$ exists along direction 2 and, consequently, for $h_{\langle\text{Cr}_2\text{O}_3\rangle} > 1$ nm [see Fig. 6(c)], misfit dislocations are also introduced along direction 2 (thereby for this case a network of perpendicular misfit dislocations develops); the dislocation distance along direction 2 slightly decreases from 34 lattice spacings \bar{c}_2 at $T_0 = 298$ K to 31 lattice spacings \bar{c}_2 at $T = 1000$ K. For the $\langle\text{Cr}_2\text{O}_3\rangle$ overgrowths on the Cr{110} and Cr{100} substrates the initial lattice mismatch along direction 2 is small (see Table VI) and all lattice mismatch along direction 2 is fully compensated by only elastic deformation even for thicknesses up to 5 nm.

The interaction contribution, $\gamma_{\langle\text{Cr}\rangle-\langle\text{Cr}_2\text{O}_3\rangle}^{\text{interaction}}$, is most negative for the $\langle\text{Cr}_2\text{O}_3\rangle$ overgrowth on the most densely packed

Cr{110} substrate (with the highest density of metal-oxygen bonds across the interface). The (partial) relaxation of the compressive growth strain in the $\langle\text{Cr}_2\text{O}_3\rangle$ film upon introduction of misfit dislocations at the $\langle\text{Cr}\rangle-\langle\text{Cr}_2\text{O}_3\rangle$ interface results in a decrease of the number of metal-oxygen bonds across the $\langle\text{Cr}\rangle-\langle\text{Cr}_2\text{O}_3\rangle$ interface per unit interface area (especially in direction 1; see above). Consequently, the aforementioned decrease of the strain contribution, $\gamma_{\langle\text{Cr}\rangle-\langle\text{Cr}_2\text{O}_3\rangle}^{\text{strain}}$, and concurrent increase of the misfit-dislocation energy contribution, $\gamma_{\langle\text{Cr}\rangle-\langle\text{Cr}_2\text{O}_3\rangle}^{i, \text{dislocation}}$, upon introduction of misfit dislocations at the $\langle\text{Cr}\rangle-\langle\text{Cr}_2\text{O}_3\rangle$ interface are accompanied by a decrease of the absolute value of the (dominating) negative interaction contribution, $\gamma_{\langle\text{Cr}\rangle-\langle\text{Cr}_2\text{O}_3\rangle}^{\text{interaction}}$, [see Eq. (4c) in Sec. II B and see Fig. 7]. Upon approaching the plastic regime, the value of $\gamma_{\langle\text{Cr}\rangle-\langle\text{Cr}_2\text{O}_3\rangle}^{\text{interaction}}$ becomes independent of $h_{\langle\text{Cr}_2\text{O}_3\rangle}$ (Fig. 7).

It is concluded that the $\langle\text{Cr}\rangle-\langle\text{Cr}_2\text{O}_3\rangle$ interfacial energy, $\gamma_{\langle\text{Cr}\rangle-\langle\text{Cr}_2\text{O}_3\rangle}$, increases with increasing oxide-film thickness (Fig. 5) mainly as a result of the associated increase of the (positive) mismatch contribution, $\gamma_{\langle\text{Cr}\rangle-\langle\text{Cr}_2\text{O}_3\rangle}^{\text{mismatch}}$. The increase of $\gamma_{\langle\text{Cr}\rangle-\langle\text{Cr}_2\text{O}_3\rangle}$ with increasing growth temperature is mainly due to the increase of the negative interaction contribution, $\gamma_{\langle\text{Cr}\rangle-\langle\text{Cr}_2\text{O}_3\rangle}^{\text{interaction}}$. It is interesting to note that this last result contrasts with the case for the temperature dependence of the $\langle\text{Al}\rangle-\langle\gamma\text{-Al}_2\text{O}_3\rangle$ interfacial energy, $\gamma_{\langle\text{Al}\rangle-\langle\gamma\text{-Al}_2\text{O}_3\rangle}$ (as calculated for the Al-Al₂O₃ system in Ref. 1), where the increase of $\gamma_{\langle\text{Al}\rangle-\langle\gamma\text{-Al}_2\text{O}_3\rangle}$ with also increasing T is dominated by the associated increase of the corresponding mismatch contribution, $\gamma_{\langle\text{Al}\rangle-\langle\gamma\text{-Al}_2\text{O}_3\rangle}^{\text{mismatch}}$ (due to the large difference in thermal expansion coefficients of the Al substrate and $\langle\gamma\text{-Al}_2\text{O}_3\rangle$ overgrowth). It is further noted that the calculated values of the interface energy (Table VII) could be compared with corresponding theoretical values as obtained by, e.g., atomistic static lattice simulation or molecular dynamics (cf. Ref. 1).

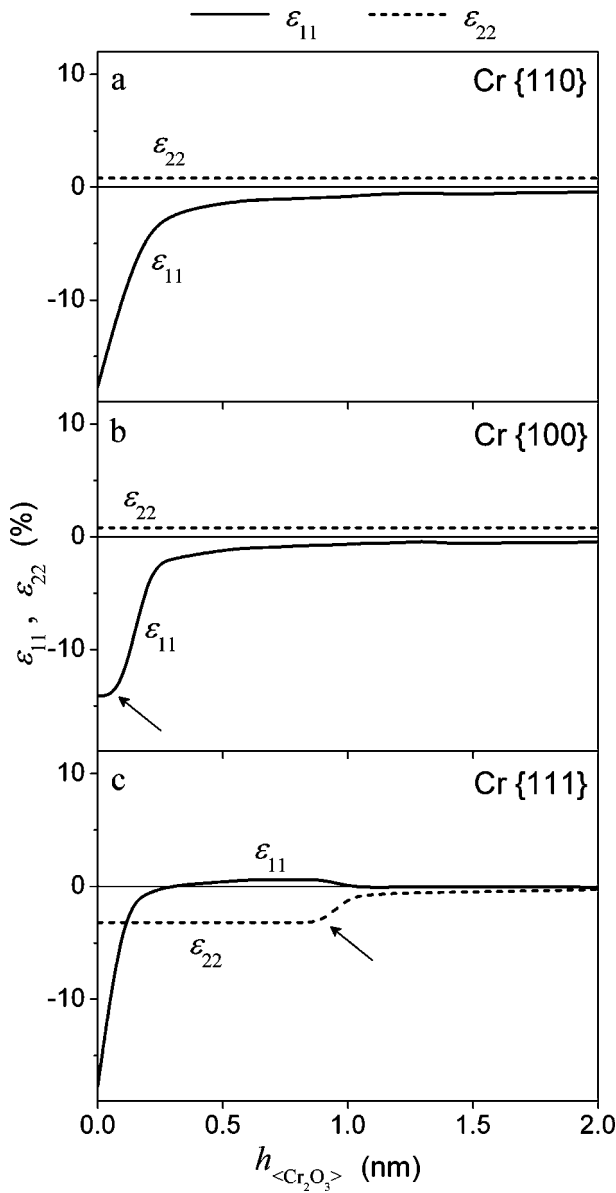


FIG. 6. Residual homogeneous strains (ϵ_{11} and ϵ_{22}) in the $\langle\text{Cr}_2\text{O}_3\rangle$ overgrowth (along the defined directions 1 and 2 parallel to the $\langle\text{Cr}\rangle$ - $\langle\text{Cr}_2\text{O}_3\rangle$ interface plane; see Table VI) as function of the crystalline oxide film thickness, $h_{\langle\text{Cr}_2\text{O}_3\rangle}$, for the overgrowth on the (a) Cr{110}, (b) Cr{100}, and (c) Cr{111} faces of the $\langle\text{Cr}\rangle$ substrate at $T_0=298$ K, as calculated (Sec. II D) using the APPR approach (Sec. II C 4).

3. Difference in interface energy of the crystalline and amorphous overgrowths

The calculated difference in interfacial energy, $\gamma_{\langle\text{Cr}\rangle\text{-}\langle\text{Cr}_2\text{O}_3\rangle} - \chi\gamma_{\langle\text{Cr}\rangle\text{-}\langle\text{Cr}_2\text{O}_3\rangle}$, for the competing cells (per unit area of the $\langle\text{Cr}\rangle$ - $\langle\text{Cr}_2\text{O}_3\rangle$ interface and for $h_{\langle\text{Cr}_2\text{O}_3\rangle}=2$ nm) has been plotted in Fig. 8 as a function of the growth temperature for the differently oriented $\langle\text{Cr}\rangle$ substrates. It follows that the interfacial energy difference is around zero for the overgrowths on the most densely packed Cr{110} substrate and negative for the other substrate orientations. Hence, the interface energy contributes to possible stabilization of an

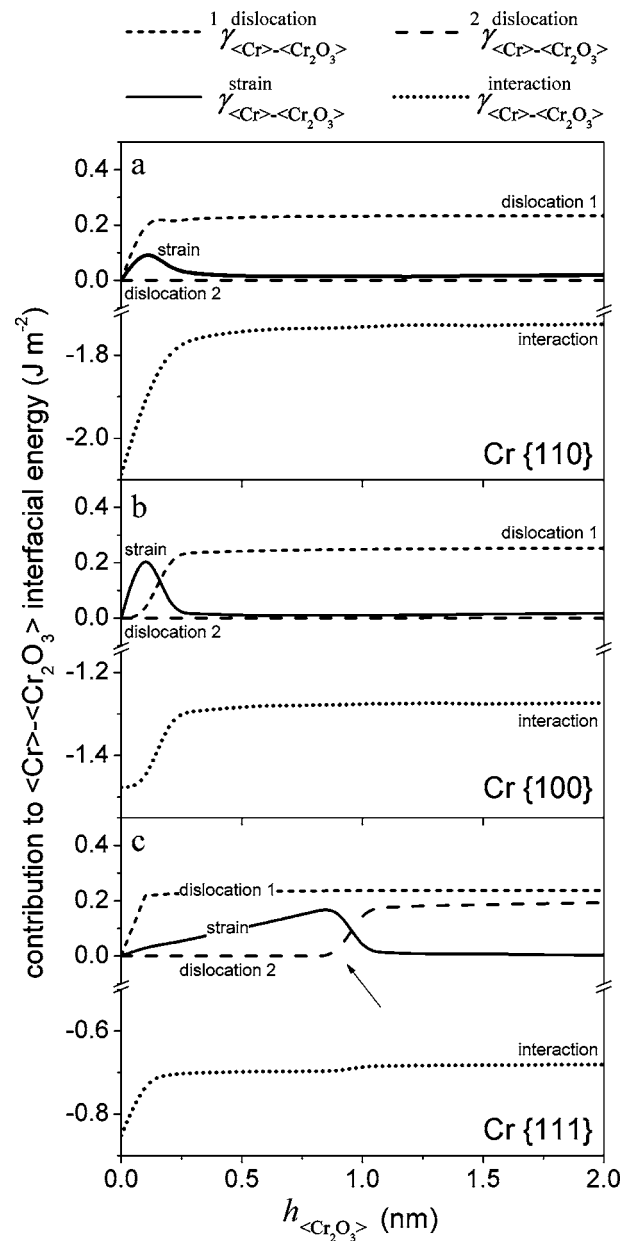


FIG. 7. Interaction, $\gamma_{\langle\text{Cr}\rangle\text{-}\langle\text{Cr}_2\text{O}_3\rangle}^{\text{interaction}}$, residual strain, $\gamma_{\langle\text{Cr}\rangle\text{-}\langle\text{Cr}_2\text{O}_3\rangle}^{\text{strain}}$, and misfit dislocation, $\gamma_{\langle\text{Cr}\rangle\text{-}\langle\text{Cr}_2\text{O}_3\rangle}^{\text{dislocation}}$ (in directions $i=1$ and 2 ; see Table V), energy contributions to the resultant $\langle\text{Cr}\rangle$ - $\langle\text{Cr}_2\text{O}_3\rangle$ interfacial energy, $\gamma_{\langle\text{Cr}\rangle\text{-}\langle\text{Cr}_2\text{O}_3\rangle}$, as function of the crystalline oxide film thickness $h_{\langle\text{Cr}_2\text{O}_3\rangle}$ at $T_0=298$ K, as calculated (Sec. II D) using the APPR approach (Sec. II C 4).

amorphous oxide film on the Cr{100} and Cr{111} substrates. The interfacial energy difference is most negative for the overgrowths on the Cr{111} substrate.

The interfacial energy difference slightly increases with increasing temperature (i.e., the crystalline $\langle\text{Cr}_2\text{O}_3\rangle$ cell becomes relatively more stable with increasing T) as a result of a relatively faster increase with temperature of the $\langle\text{Cr}\rangle$ - $\langle\text{Cr}_2\text{O}_3\rangle$ interfacial energy. The thickness-dependence of the interfacial energy difference (not shown here) is governed by the thickness-dependence of the $\langle\text{Cr}\rangle$ - $\langle\text{Cr}_2\text{O}_3\rangle$ interfacial energy, as discussed in Sec. III C 2, thereby stabilizing the

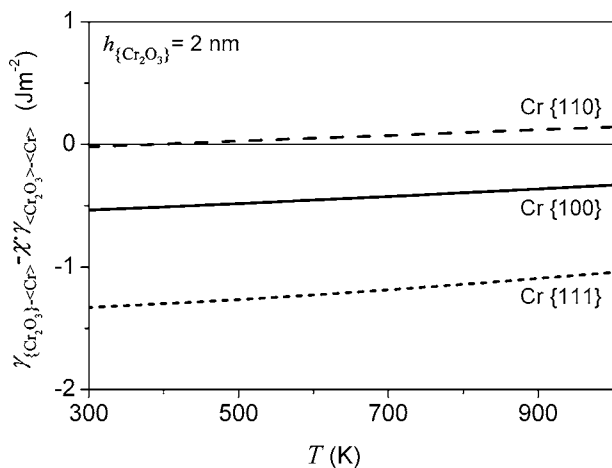


FIG. 8. Interfacial energy difference, $\gamma_{\langle Cr_2O_3 \rangle - \langle Cr \rangle} - \chi \gamma_{\langle Cr_2O_3 \rangle - \langle Cr \rangle}$, [per unit area of the $\langle Cr \rangle - \langle Cr_2O_3 \rangle$ interface; see Eq. (1)] as function of the growth temperature, T , for the competing amorphous $\{Cr_2O_3\}$ and crystalline $\langle Cr_2O_3 \rangle$ cells on the $\{110\}$, $\{100\}$, and $\{111\}$ faces of the $\langle Cr \rangle$ substrate within the plastic regime (i.e., for a thickness of the $\{Cr_2O_3\}$ overgrowth of $h_{\{Cr_2O_3\}} = 2$ nm). The $\langle Cr \rangle - \langle Cr_2O_3 \rangle$ interfacial energy has been calculated according to the numerical procedure outlined in Sec. II D, while employing the APPR approach for the estimation of the misfit-dislocation energy contribution, $\gamma_{\langle Cr \rangle - \langle Cr_2O_3 \rangle}^{dislocation}$ (see Sec. II C 4).

$\{Cr_2O_3\}$ cell with increasing thickness in the elastic and mixed regime (in the plastic regime, the interfacial energy difference is independent of the film thickness; see Sec. III C 2 and Fig. 7).

Here it is noted that the outcome of the model calculations as presented in Sec. IV A is only sensitive to the interface energy differences between the cases of amorphous and crystalline oxide overgrowths (i.e., the outcome of the model calculations is less sensitive to systematic errors in the absolute values of the interface energies; see Tables IV and VII).

IV. RELATIVE STABILITIES OF AMORPHOUS AND CRYSTALLINE OXIDE FILMS

A. Model predictions

An amorphous nature for the oxide film is preferred over a crystalline modification if $\Delta G = G_{\{Cr_2O_3\}} - G_{\langle Cr_2O_3 \rangle} < 0$ (see Sec. II). Defining the critical thickness, $h_{\{Cr_2O_3\}}^{critical}$, as the thickness of the amorphous cell for which $\Delta G = 0$ (i.e., $G_{\{Cr_2O_3\}} = G_{\langle Cr_2O_3 \rangle}$), then for $h_{\{Cr_2O_3\}} < h_{\{Cr_2O_3\}}^{critical}$ the thermodynamically most stable substrate/overgrowth configuration is the amorphous one, whereas for $h_{\{Cr_2O_3\}} > h_{\{Cr_2O_3\}}^{critical}$ the crystalline $\langle Cr_2O_3 \rangle$ cell is thermodynamically preferred. The value of $h_{\{Cr_2O_3\}}^{critical}$ has been calculated as a function of the growth temperature and the $\langle Cr \rangle$ substrate orientation by application of Eq. (1) and using the results for the bulk, surface and interfacial energies presented in Sec. III. These final results are shown in Fig. 9. Because of the minimization procedure implemented to calculate the $\langle Cr \rangle - \langle Cr_2O_3 \rangle$ interfacial energy [see Eq. (13) in Sec. II D], an analytical expression for the

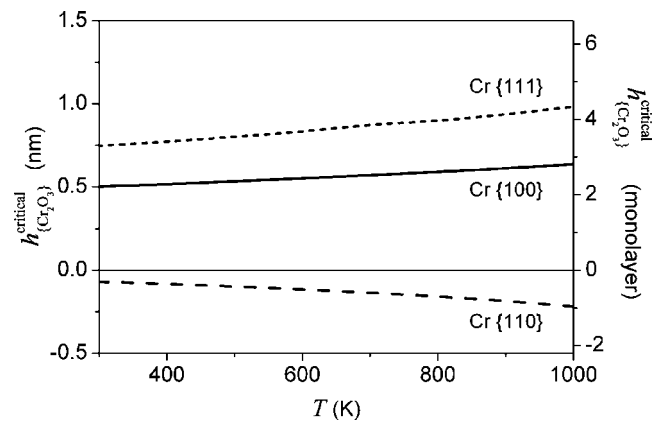


FIG. 9. The critical oxide-film thickness, $h_{\{Cr_2O_3\}}^{critical}$, up to which an amorphous $\{Cr_2O_3\}$ overgrowth instead of a crystalline $\langle Cr_2O_3 \rangle$ overgrowth is thermodynamically preferred on the $\{110\}$, $\{100\}$, and $\{111\}$ faces of a single-crystalline $\langle Cr \rangle$ substrate as function of the growth temperature, T .

critical thickness, $h_{\{Cr_2O_3\}}^{critical}$, (as presented in Ref. 1 for the elastic regime) cannot be given here.

It is concluded that (see Fig. 9) the onset of oxidation on the bare $Cr\{100\}$ and $Cr\{111\}$ substrates is predicted to proceed by the direct formation and growth of an amorphous $\{Cr_2O_3\}$ oxide film up to a critical thickness of about 0.5 and 0.8 nm at $T_0 = 298$ K, and up to a critical thickness of about 0.6 and 1 nm at $T = 1000$ K, respectively. Thus the amorphous $\{Cr_2O_3\}$ film is most stable on the *least* densely-packed $Cr\{111\}$ surface. The amorphous $\{Cr_2O_3\}$ film on the $Cr\{100\}$ and $Cr\{111\}$ substrates is stabilized, as compared to the crystalline modification, by the lower sum of the surface and interfacial energies for the amorphous configuration, with the relative contribution of the surface energy difference predominating for the overgrowth on the $Cr\{100\}$ substrate, whereas the surface and interfacial energy differences are about equal for the overgrowth on the $Cr\{111\}$ substrate (compare Figs. 4 and 8).

A negative critical thickness, $h_{\{Cr_2O_3\}}^{critical}$, is obtained for the overgrowth on the bare $Cr\{110\}$ substrate, which implies that the onset of oxidation on the *most* densely-packed Cr surface is predicted to proceed by the direct formation and growth of a semicoherent crystalline $\langle Cr_2O_3 \rangle$ oxide. In this case the positive bulk Gibbs energy difference between the amorphous and crystalline cells (see Fig. 3) cannot be compensated solely by the relatively lower surface energy of the amorphous $\{Cr_2O_3\}$ cell on the $Cr\{110\}$ substrate (see Fig. 4).

The critical thickness increases more strongly with temperature T for the $Al-Al_2O_3$ system (see Fig. 6 in Ref. 1), which is due to the relative large difference in thermal expansion coefficient between the Al substrate and the Al_2O_3 overgrowth (which results in a strong increase of the initial lattice mismatch with increasing T ; cf., the end of Sec. III C 2).

B. Experimental observations versus model predictions

For the thermal oxidation of a bare, single-crystalline $Cr\{111\}$ substrate at room temperature, the development of

an amorphous Cr-oxide (of thickness 0.9 nm) has been reported, as deduced from the shape of valence band spectra of the oxidized metal as recorded using UPS and XPS.¹³ For the corresponding oxidations at an elevated temperature of 773 K, instead an epitaxial crystalline Cr₂O₃ film of thickness ~4.1 nm has been reported.¹³ Both these observations are in full agreement with the present model predictions (Fig. 9).

The available microstructural observations of the initial oxide developing on the bare Cr{100} substrate are very ambiguous:^{7,9,11} Whereas the formation of an initial amorphous oxide film at 1073 K is suggested by LEED,⁹ corresponding observations by RHEED are indicative of the formation of a polycrystalline oxide film at $T=773$ K (Ref. 7) and $T>873$ K.¹¹

In full agreement with the model predictions, the direct formation of a semicoherent crystalline oxide film has been observed for the bare Cr{110} surface by x-ray scattering,¹² LEED,^{7,8} and RHEED (Ref. 10) upon thermal oxidation at various temperatures (in the range of 463 K–1173 K) and for various oxide-film thicknesses (in the range of 2–5 nm). Also, the coherent Cr₂O₃ film grown at $T=1173$ K showed LEED spots characteristic of the Cr₂O₃{0001} surface (as employed in the current model calculations; see Sec. III B).⁷ Moreover, a layer-by-layer growth mode has been indicated on the basis of reflectivity measurements for the 4.4 nm thick, epitaxial oxide film grown at 603 K.¹²

V. CONCLUSION

A conclusive description of the thermodynamics of initial oxide-film growth on a bare, single-crystalline metal substrate, $\langle M \rangle$, is only obtained if the role of interface and surface energies is accounted for. On such a basis a meaningful comparison of the relative stabilities of amorphous and crystalline modifications of the oxide overgrowth, $\{MO_x\}$ and $\langle MO_x \rangle$, respectively, can be made.

For the assessment of the $\langle M \rangle$ - $\langle MO_x \rangle$ interface energy, the relaxation of elastic growth strain in the crystalline overgrowth by introduction of misfit dislocations at the $\langle M \rangle$ - $\langle MO_x \rangle$ interface (i.e., by plastic deformation) has now been accounted for in the thermodynamic modeling. The total interface energy of the $\langle M \rangle$ - $\langle MO_x \rangle$ interface can be conceived as the resultant of three additive energy contributions due to (i) the chemical bonding between the oxide overgrowth and the metal substrate across the $\langle M \rangle$ - $\langle MO_x \rangle$ interface, (ii) the residual homogeneous strain in the semicoherent, crystalline oxide film, and (iii) the misfit dislocations at the $\langle M \rangle$ - $\langle MO_x \rangle$ interface. The misfit dislocation configuration of and

the residual strain in the developing crystalline oxide film follow from the minimum value of the $\langle M \rangle$ - $\langle MO_x \rangle$ interface energy, as determined iteratively.

Comparing and evaluating various models for crystalline misfit accommodation, the “first approximation” approach was found to be a most suitable model for estimation of the energy of an array network of misfit dislocations in the oxide overgrowth for a wide range of initial lattice-mismatch values in both the monolayer and nanometer thickness regimes. Application of the corresponding “semi-infinite overgrowth,” “large dislocation distance,” “extrapolation,” and “Volterra” approaches is restricted to metal-substrate/oxide-film systems with small initial lattice mismatches and/or to thick overgrowths within the plastic regime, whereas application of the “Ball” approach is confined to the monolayer thickness regime.

Evaluation of the thermodynamic model on this basis for an oxide film growing on a metal substrate shows that the relatively high bulk Gibbs energy for the amorphous oxide film can be more than compensated by its relatively low sum of surface and interface energies.

For the case of crystalline oxide overgrowths on the {111}, {110}, and {100} crystallographic faces of a bare single-crystalline Cr substrate, misfit dislocations are introduced at already the onset of the growth along the direction (in the interface plane) of high initial lattice mismatch (i.e., $|f| > 14\%$). Only for the crystalline oxide overgrowth on the Cr{111} substrate, a second array of misfit dislocations is introduced in the corresponding perpendicular direction of low initial lattice mismatch (i.e., $|f| > 3\%$) for film thicknesses >1 nm, whereas for the Cr{110} and Cr{100} substrates, the relatively small lattice mismatch (i.e., 0.8%) in the second direction is accommodated fully elastically up to film thicknesses of at least 5 nm.

The thermodynamic model applied to the onset of oxide-film growth on the relatively less-densely packed Cr{111} and Cr{100} substrates predicts the direct formation and growth of an amorphous $\{Cr_2O_3\}$ film up to a critical thickness of about 3 to 5 oxide monolayers (i.e., 0.5–1 nm) in the temperature range of 398–1000 K; beyond the critical thickness the crystalline modification is more stable than the amorphous one. Similarly it is predicted that oxide-film growth on the most-densely packed Cr{110} substrate starts with the formation and growth of a semicoherent crystalline oxide film that exhibits a strong anisotropic, elastic growth strain. These predicted energetics of the oxide films grown on the differently oriented Cr substrates provide a thermodynamic (rather than kinetic) explanation of the experimental observations.

*Email address: l.p.h.jeurgens@mf.mpg.de

¹L. P. H. Jeurgens, W. G. Sloof, F. D. Tichelaar, and E. J. Mittemeijer, Phys. Rev. B **62**, 4707 (2000).

²F. P. Fehlner, *Low-temperature Oxidation: The Role of Vitreous Oxides* (Wiley-Interscience, New York, 1986).

³I. E. Wachs, Catal. Today **100**, 79 (2005).

⁴A. Johansson, G. Sambandamurthy, D. Shahar, N. Jacobson, and R. Tenne, Phys. Rev. Lett. **95**, 116805 (2005).

⁵C. J. Först, K. Schwarz, and P. E. Blöchl, Phys. Rev. Lett. **95**, 137602 (2005).

- ⁶A. Tschöpe, *J. Electroceram.* **14**, 5 (2005).
- ⁷P. Michel and Ch. Jardin, *Surf. Sci.* **36**, 478 (1973).
- ⁸H. Ma, Y. Berthier, and P. Marcus, *Appl. Surf. Sci.* **153**, 40 (1999).
- ⁹C. A. Haque and H. E. Farnsworth, *Surf. Sci.* **1**, 378 (1964).
- ¹⁰H. M. Kennett and A. E. Lee, *Surf. Sci.* **33**, 377 (1972).
- ¹¹J. S. Arlow, D. F. Mitchell, and M. J. Graham, *J. Vac. Sci. Technol. A* **5**, 572 (1987).
- ¹²A. Stierle, P. Bödeker, and H. Zabel, *Surf. Sci.* **327**, 9 (1995).
- ¹³G. Gewinner, J. C. Peruchetti, A. Jaéglé, and A. Kalt, *Surf. Sci.* **78**, 439 (1978).
- ¹⁴F. R. de Boer, R. Boom, W. C. M. Mattens, A. R. Miedema, and A. K. Niessen, *Cohesion in Metals: Transition Metals Alloys* (North-Holland, Amsterdam, 1989), Chaps. 2 and 4.
- ¹⁵S. H. Oh, Y. Kauffmann, C. Scheu, W. D. Kaplan, and M. Rühle, *Science* **310**, 661 (2005).
- ¹⁶If the lateral extent of the oxide film is not infinite, as is the case for e.g., coherent oxide islands on the bare metal surface, a heterogeneous strain occurs in the oxide. For the very thin oxide overgrowths (<5 nm) considered in this study, it may be assumed that the system (i.e., metal and oxide film) is of infinite length in the directions parallel to the metal-oxide interface. It then follows that a homogeneous strain resides within the oxide overgrowth.
- ¹⁷C. A. B. Ball, *Phys. Status Solidi* **42**, 357 (1970).
- ¹⁸J. H. van der Merwe, *Surf. Sci.* **31**, 198 (1972).
- ¹⁹J. H. van der Merwe, *J. Appl. Phys.* **34**, 117 (1963); **34**, 123 (1963); **34**, 3420(E) (1963).
- ²⁰J. H. van der Merwe, in *Single Crystal Films*, edited by M. H. Francombe and H. Sato (Pergamon Press, Oxford, 1964), p. 139.
- ²¹J. H. van der Merwe and W. A. Jesser, *J. Appl. Phys.* **64**, 4968 (1988).
- ²²J. H. van der Merwe and N. G. van der Berg, *Surf. Sci.* **32**, 1 (1972).
- ²³J. H. van der Merwe, *J. Appl. Phys.* **41**, 4725 (1970).
- ²⁴J. W. Matthews, *J. Vac. Sci. Technol.* **12**, 126 (1975).
- ²⁵J. W. Matthews, in *Dislocation in Solids*, edited by F. R. N. Nabarro (North-Holland, Amsterdam, 1979), Vol. 2, Chap. 7, p. 461.
- ²⁶Since the dislocations form regular arrays the crystals can be considered as almost perfect and entropy differences play an insignificant role in the following considerations (Ref. 11).
- ²⁷MATLAB version 6.1.0.450, Release 12.1 (The MathWorks Inc., Natick, 2001).
- ²⁸Powder Diffraction Files, Cards 89-4055 and 82-1484 from JCPDS-International Centre for Diffraction Data (2001).
- ²⁹M. W. Chase, *J. Phys. Chem. Ref. Data* **9**, 959 (1998); M. W. Chase, Jr., *NIST-JANAF Thermochemical Tables 4th Ed., Part II. Cr-Zr* (American Institute of Physics, New York, 1998).
- ³⁰C. Jardin and P. Michel, *Surf. Sci.* **71**, 575 (1978).
- ³¹F. Reichel, L. P. H. Jeurgens, and E. J. Mittemeijer (unpublished).
- ³²N. Zouvelou, D. Skarmoutsos, and P. Nikolopoulos, *Key Eng. Mater.* **264**, 679 (2004).
- ³³D. T. Livey and P. Murray, *J. Am. Ceram. Soc.* **39**, 363 (1956).
- ³⁴P. J. Lawrence, S. C. Parker, and P. W. Tasker, *J. Am. Ceram. Soc.* **71**, C-389 (1988).
- ³⁵R. G. Linford, *Chem. Soc. Rev.* **1**, 445 (1972).
- ³⁶Y. S. Touloukian, R. K. Kirby, R. E. Taylor, and T. Y. R. Lee, *Thermophysical Properties of Matter: Thermal Expansion; Elements and Alloy* (IFI/Plenum, New York, 1977), Vol. 12, p. 61.
- ³⁷Y. S. Touloukian, R. K. Kirby, R. E. Taylor, and T. Y. R. Lee, *Thermophysical Properties of Matter: Thermal Expansion; Non-metallic Solids* (IFI/Plenum, New York, 1977), Vol. 13, p. 217.
- ³⁸L. Vitos, A. V. Ruban, H. L. Skriver, and J. Kollár, *Surf. Sci.* **411**, 186 (1998).
- ³⁹J.-M. Zhang, F. Ma, and K.-W. Xu, *Surf. Interface Anal.* **35**, 662 (2003).
- ⁴⁰B.-J. Lee, M. I. Baskes, H. Kim, and Y. K. Cho, *Phys. Rev. B* **64**, 184102 (2001).
- ⁴¹H. Wawra, *Z. Metallkd.* **66**, 395 (1975).
- ⁴²H. L. Alberts and J. C. A. Boeyens, *J. Magn. Magn. Mater.* **2**, 327 (1976).
- ⁴³G. Simmons, *Single Crystal Elastic Constants and Calculated Aggregate Properties: A Handbook* 2nd edition (M.I.T. Press, Cambridge, Massachusetts, 1971), p. 20.